# The ECCO-Darwin Data-Assimilative Global Ocean Biogeochemistry Model: Estimates of Seasonal to Multidecadal Surface Ocean $pCO_2$ and Air-Sea $CO_2$ Flux

D. Carroll[1,2] , D. Menemenlis[2] , J. F. Adkins[3] , K. W. Bowman[2] , H. Brix[4,5] , S. Dutkiewicz[6,7] , I. Fenty[2] , M. M. Gierach[2] , C. Hill[6] , O. Jahn[6] , P. Landschützer[8] , J. M. Lauderdale[6] , J. Liu[2] , M. Manizza[9] , J. D. Naviaux[3] , C. Rödenbeck[10] , D. S. Schimel[2] , T. Van der Stocken[2] , and H. Zhang[2]

[1]Moss Landing Marine Laboratories, San José State University, Moss Landing, CA, USA, [2]Jet Propulsion Laboratory, California Institute of Technology, Pasadena, CA, USA, [3]Division of Geological and Planetary Sciences, California Institute of Technology, Pasadena, CA, USA, [4]Institute of Coastal Research, Helmholtz-Zentrum Geesthacht, Geesthacht, Germany, [5]Joint Institute for Regional Earth System Science and Engineering, University of California, Los Angeles, Los Angeles, CA, USA, [6]Department of Earth, Atmospheric and Planetary Sciences, Massachusetts Institute of Technology, Cambridge, MA, USA, [7]Center for Global Change Science, Massachusetts Institute of Technology, Cambridge, MA, USA, [8]Max Planck Institute for Meteorology, Hamburg, Germany, [9]Geosciences Research Division, Scripps Institution of Oceanography, University of California, San Diego, La Jolla, CA, USA, [10]Max Planck Institute for Biogeochemistry, Jena, Germany

**Abstract** Quantifying variability in the ocean carbon sink remains problematic due to sparse observations and spatiotemporal variability in surface ocean $pCO_2$. To address this challenge, we have updated and improved ECCO-Darwin, a global ocean biogeochemistry model that assimilates both physical and biogeochemical observations. The model consists of an adjoint-based ocean circulation estimate from the Estimating the Circulation and Climate of the Ocean (ECCO) consortium and an ecosystem model developed by the Massachusetts Institute of Technology Darwin Project. In addition to the data-constrained ECCO physics, a Green's function approach is used to optimize the biogeochemistry by adjusting initial conditions and six biogeochemical parameters. Over seasonal to multidecadal timescales (1995–2017), ECCO-Darwin exhibits broad-scale consistency with observed surface ocean $pCO_2$ and air-sea $CO_2$ flux reconstructions in most biomes, particularly in the subtropical and equatorial regions. The largest differences between $CO_2$ uptake occur in subpolar seasonally stratified biomes, where ECCO-Darwin results in stronger winter uptake. Compared to the Global Carbon Project OBMs, ECCO-Darwin has a time-mean global ocean $CO_2$ sink ($2.47 \pm 0.50$ Pg C year$^{-1}$) and interannual variability that are more consistent with interpolation-based products. Compared to interpolation-based methods, ECCO-Darwin is less sensitive to sparse and irregularly sampled observations. Thus, ECCO-Darwin provides a basis for identifying and predicting the consequences of natural and anthropogenic perturbations to the ocean carbon cycle, as well as the climate-related sensitivity of marine ecosystems. Our study further highlights the importance of physically consistent, property-conserving reconstructions, as are provided by ECCO, for ocean biogeochemistry studies.

**Plain Language Summary** Data-driven estimates of how much carbon dioxide the ocean is absorbing (the so-called "ocean carbon sink") have improved substantially in recent years. However, computational ocean models that include biogeochemistry continue to play a critical role as they allow us to isolate and understand the individual processes that control ocean carbon sequestration. The ideal scenario is a combination of the above two methods, where data are ingested and then used to improve a model's fit to the observed ocean, also known as, data assimilation. While the physical oceanographic community has made great progress in developing data assimilation systems, for example, the Estimating the Circulation and Climate of the Ocean (ECCO) consortium, the biogeochemical community has generally lagged behind. The ECCO-Darwin model presented in this paper represents an important technological step forward as it is the first global ocean biogeochemistry model that (1) ingests both physical and biogeochemical observations into the model in a realistic manner and (2) considers how the nature of the ocean carbon sink has changed over multiple decades. As the ECCO ocean circulation

estimates become more accurate and lengthen in time, ECCO-Darwin will become an ever more accurate and useful tool for climate-related ocean carbon cycle and mitigation studies.

## 1. Introduction

The ocean plays a vital role in regulating the global climate system and mitigating climate change. This has motivated numerous studies to quantify and monitor trends and patterns in the oceanic sink of atmospheric carbon dioxide ($CO_2$), which has absorbed roughly 48% of anthropogenic $CO_2$ emissions during 1800–1994 (Sabine et al., 2004). For example, based on a survey of inorganic carbon distribution in the 1990s, the global oceanic carbon uptake has been estimated at $118 \pm 19$ Pg C year$^{-1}$. More recent estimates have been inferred from model-based methods, yielding mean uptake rates of $2.3 \pm 0.6$ Pg C year$^{-1}$ (Khatiwala et al., 2009) and $2.6 \pm 0.3$ Pg C year$^{-1}$ (Gruber et al., 2019). Although results from these studies suggest an increase in oceanic $CO_2$ uptake over the last several decades (DeVries, 2014; DeVries et al., 2017, 2019; Khatiwala et al., 2013; Sarmiento & Gruber, 2002), storage rates may depend on complex biologically driven feedbacks (Riebesell et al., 2007) and show considerable spatial variability (Gruber et al., 2019), rendering the long-term efficiency of the ocean $CO_2$ sink uncertain (Landschützer et al., 2015; Le Quéré et al., 2010; Munro et al., 2015). Quantifying the magnitude and time-space variability of the oceanic $CO_2$ sink has been recognized as an important goal in the Fifth Assessment Report of the Intergovernmental Panel on Climate Change (IPCC, 2013). Addressing this goal will improve predictions of the future climate trajectory, assist in the formulation of climate-related policies, and help implement mitigation and adaptation strategies.

As the global carbon budget represents the time-space integration of small-scale processes, a mechanistic understanding of the regional drivers of air-sea $CO_2$ exchange (Lovenduski et al., 2016) at seasonal to multi-decadal timescales is required for assessing the response and potential vulnerability of the oceanic $CO_2$ sink to climate change (Ciais et al., 2013). Although $CO_2$ exchange across the air-sea interface is difficult to measure directly, observations of oceanic and atmospheric partial pressure of carbon dioxide ($p$CO$_2$) have increased rapidly over the last decade (Bakker et al., 2014; Pfeil et al., 2013; Takahashi et al., 2009). However, these measurements remain sparse and exhibit weak temporal and spatial coherence, preventing their use in estimating oceanic $CO_2$ sink variability over the time-space scales required for detecting anthropogenic trends (McKinley et al., 2016). This is especially problematic given that air-sea $CO_2$ fluxes also exhibit substantial spatiotemporal variability (Fay & McKinley, 2013; Gray et al., 2018; Gruber et al., 2002; Lovenduski et al., 2015; Wanninkhof et al., 2013). Furthermore, multidecadal time series of surface ocean $p$CO$_2$ only exist at a few locations in the global ocean (e.g., the Tropical Atmosphere Ocean Array, Hawaii Ocean Time Series, and Bermuda Atlantic Timeseries Study) (Bates et al., 2014; Dore et al., 2009; Feely et al., 2006).

To address these deficiencies, extensive efforts have been made to combine internally consistent databases of surface ocean $p$CO$_2$ measurements with gas transfer velocity parameterizations (Wanninkhof, 1992) and various interpolation methods, resulting in global maps of surface ocean $p$CO$_2$ and air-sea $CO_2$ flux (Landschützer et al., 2014, 2016; Rödenbeck et al., 2013; Takahashi et al., 2002, 2009). However, despite the broad-scale consistency between these interpolation-based products, particularly in the equatorial Pacific Ocean (Rödenbeck et al., 2015), estimates from these methods suffer from a number of methodological uncertainties and uneven observational sampling (Fay et al., 2014), which can lead to diverging results in data-sparse regions (e.g., the Arctic and Southern Ocean) (Ritter et al., 2017; Rödenbeck et al., 2015; Schuster et al., 2013).

In contrast to interpolation-based methods, ocean biogeochemical models (OBMs) (Aumont et al., 2015; Galbraith et al., 2010; Stock et al., 2014) have the ability to resolve the spatiotemporal scales necessary for attributing air-sea $CO_2$ fluxes to their respective mechanisms (Ito & Follows, 2013; Lauderdale et al., 2016; Takahashi et al., 2002). Numerous hindcast OBMs, forced with time-varying atmospheric boundary conditions, have been previously used to assess oceanic $CO_2$ sink variability (Le Quéré et al., 2003, 2018; Sarmiento et al., 2010), but these models do not assimilate physical and biogeochemical observations. Additionally, data-assimilative OBMs either are limited to regional studies (e.g., the Southern Ocean, Verdy & Mazloff, 2017) or have global coverage but are integrated over short time periods (e.g., 2009–2011,

Brix et al., 2015). With the advent of global carbon cycle data assimilation systems, such as the National Aeronautics and Space Administration Carbon Monitoring System Flux project (Bowman et al., 2017; Liu et al., 2014, 2017), there is a need for data-assimilative OBMs that resolve fine-scale regional patterns of air-sea $CO_2$ flux over seasonal to multidecadal timescales.

In this paper, we describe our efforts to update and improve ECCO-Darwin, a global ocean biogeochemistry model that assimilates both physical and biogeochemical observations. ECCO-Darwin is based on (1) an adjoint-based ocean circulation estimate provided by the Estimating the Circulation and Climate of the Ocean (ECCO) consortium and (2) a realistic ecosystem model provided by the Massachusetts Institute of Technology (MIT) Darwin Project. Here we significantly improve ECCO-Darwin from the pilot study of Brix et al. (2015) by extending the time coverage to multiple decades (1995–2017) and addressing important issues such as an arbitrary constraint on the global-mean carbon uptake and exaggerated seasonal and synoptic variability in Southern Ocean air-sea $CO_2$ fluxes. We use a low-dimensional Green's function approach to adjust initial conditions and biogeochemical parameters (six). This optimizes the model's fit to observations in a property-conserving manner (i.e., without nudging or creating artificial sources/sinks), resulting in a quantitative description of the time-varying global ocean biogeochemical state that is ideal for ocean carbon budget studies. Finally, we use this updated version of ECCO-Darwin, along with complementary interpolation-based products, to provide global and biome-scale estimates of seasonal to multidecadal surface ocean $p$CO$_2$ and air-sea $CO_2$ flux variability.

## 2. Methods

### 2.1. Overview

The ECCO-Darwin OBM (henceforth referred to as ED) described in this paper is based on a global ocean and sea ice configuration of the MIT general circulation model (MITgcm) (Marshall et al., 1997) and on the pilot study described in Brix et al. (2015). The physical ocean circulation is from the ECCO consortium (Wunsch et al., 2009), which synthesizes the MITgcm with nearly all available ocean observations since the era of satellite altimetry (~1992), and provides an adjoint-based reconstruction of the three-dimensional, time-varying global ocean and sea ice state. The ECCO circulation estimates are coupled online with the MIT Darwin ecosystem model (Dutkiewicz et al., 2009, 2014; Follows et al., 2007; Follows & Dutkiewicz, 2011), which in turn drives and interacts with marine chemistry variables. Instructions for building and running ED are given in supporting information Text S1.

### 2.2. ED Physical Model

For the ED physical fields, we use the ECCO LLC270 global ocean and sea ice data synthesis (Zhang et al., 2018). ECCO LLC270 is built upon two previous ECCO efforts, ECCO v4 (Forget et al., 2015), and ECCO2 (Fenty et al., 2017; Menemenlis et al., 2008). Compared to the lower-resolution ECCO v4 synthesis (nominal 1° grid spacing), ECCO LLC270 has finer horizontal grid spacing (~1/3° at the equator and ~18 km at high latitudes). The vertical discretization comprises 50 $z$ levels; model integration spans January 1992 to December 2017. Terrestrial runoff along coastal boundaries is forced using the monthly climatology of Fekete et al. (2002). Since horizontal resolution is insufficient to resolve mesoscale eddies, their impact on the large-scale ocean circulation is parameterized using the Redi (1982) and Gent and McWilliams (1990) schemes.

Remotely sensed data constraints include daily along-track sea level anomalies from satellite altimetry (Forget & Ponte, 2015) relative to a mean dynamic topography (Andersen et al., 2016), monthly ocean bottom pressure anomalies from the Gravity Recovery and Climate Experiment mission (Watkins et al., 2015), daily sea surface temperature (SST) (Reynolds et al., 2002), and sea ice concentration fields from passive microwave radiometry (Meier et al., 2017). The primary in situ data constraints include the global array of Argo floats (Riser et al., 2016; Roemmich & Gilson, 2009), ship-based hydrography incorporated as monthly climatological temperature and salinity profiles from the World Ocean Atlas 2009 (Antonov et al., 2010; Locarnini et al., 2010), tagged marine mammals (Roquet et al., 2013; Treasure et al., 2017), and ice-tethered profilers in the Arctic (Krishfield et al., 2008).

To fit the above observations, the ECCO LLC270 solution minimizes a weighted quadratic sum of model data differences. This is done using the adjoint method, also known as 4-D-Var (see Wunsch &

Heimbach, 2013; Wunsch et al., 2009). The control variables include initial temperature and salinity fields; time-invariant diapycnal, Redi (1982)-isopycnal, and Gent and McWilliams (1990)-thickness diffusivities; and 14-day adjustments to the 6-hourly ERA Interim (Dee et al., 2011) estimates of downward shortwave and longwave radiation, precipitation, 2-m air temperature and specific humidity, and 10-m zonal and meridional wind. In this way, ECCO LLC270 provides a physically consistent, property-conserving reconstruction of the three-dimensional, time-evolving ocean and sea ice state. The specific state estimate used in this manuscript is not fully optimized: it is the result of 42 forward-adjoint iterations. Nevertheless, the cost function has been reduced by 85% relative to the unconstrained (iteration 0) simulation. A detailed evaluation of the ECCO LLC270 iteration-42 state estimate, the so-called "ECCO standard analysis" of Forget et al. (2015), is made available as Data Set S1 in the supporting information. Because the initial conditions are estimated as part of the optimization procedure, the ECCO LLC270 state estimate has negligible drift and therefore does not require spin up.

Although not yet fully optimized, the ECCO LLC270 state estimate has begun to be employed in a small number of early studies. In particular, it is being used as lateral boundary conditions for several published (e.g., Khazendar et al., 2019; Nakayama et al., 2017, 2018, 2019; Wood et al., 2018) and underway regional studies. The present study is the first utilization of ECCO LLC270 in a global context. The importance of a data-constrained, property-conserving ocean state estimate for OBMs cannot be overstated. For example, Table 1 in Mikaloff Fletcher et al. (2006) shows that even a very early, coarse-resolution ECCO state estimate (Stammer et al., 2004) achieved skill comparable to, or greater than, that of more established and specialized OBMs. The ECCO LLC270 state estimate is substantially improved compared to the state estimate of Stammer et al. (2004), not only because of increased horizontal/vertical grid resolution and the inclusion of the Arctic Ocean and sea ice but also because the earlier solution did not include adjustments for model subgrid-scale parameterizations. Compared to the state estimate used in Brix et al. (2015), the LLC270 state estimate does not admit mesoscale eddies; however, it is of substantially longer duration (26 vs. 2 years) and, again because of subgrid-scale adjustments, is closer to observations. Additionally, the ECCO project is actively working on higher-quality, higher-resolution ocean state estimates so that the quality and realism of the ECCO-Darwin OBM will continue to improve as new physical state estimates become available.

### 2.3. ED Biogeochemistry Model

To couple the ED physical model with ocean ecology and carbon chemistry, we use the MIT Darwin Project ecosystem model previously described in Brix et al. (2015). The ED biogeochemistry includes 39 prognostic variables (supporting information Table S1) that are advected and mixed by the ECCO LL270 physical fields; currently, there are no feedbacks between biogeochemistry and circulation, such as light absorption and bio-mixing effects (Kunze, 2019). The coupling between ocean physics and biogeochemistry is done online at every model time step (1,200 s). The simplified Darwin ecology includes five large-to-small phytoplankton function types (diatoms, other large eukaryotes, *Synechococcus*, and low- and high-light adapted *Prochlorococcus*) and two zooplankton types that graze preferentially on either the large eukaryotes or small picoplankton. The carbon cycle is explicitly represented, along with nitrogen, phosphorus, iron, silica, oxygen, and alkalinity; carbonate chemistry is based on the efficient solver of Follows et al. (2006). Air-sea $CO_2$ flux is computed using the parameterization of Wanninkhof (1992) and atmospheric $p\text{CO}_2$ from the zonally averaged monthly National Oceanic and Atmospheric Administration Marine Boundary Layer Reference product (Andrews et al., 2014). Atmospheric iron dust deposition at the ocean surface is forced using the monthly climatology of Mahowald et al. (2009). To prevent unrealistic accumulation of particulates in bathymetric "wells" (i.e., wet grid cells surrounded horizontally by dry cells) on the model grid, we added a porous bottom boundary condition (i.e., all particulates are instantly removed once they reach the seafloor). We stress that all tracers, both physical and biogeochemical, are conserved within model numerical precision from the initial conditions to the end of the simulation.

### 2.4. ED Biogeochemical Improvements and Optimization

The biogeochemical observations used to evaluate and adjust ED include (1) surface ocean fugacity ($f\text{CO}_2$) from the monthly gridded Surface Ocean $CO_2$ Atlas (SOCATv5, Bakker et al., 2016), (2) GLODAPv2 ship-based profiles of $NO_3$, $PO_4$, $SiO_2$, $O_2$, dissolved inorganic carbon (DIC) derived from pH and alkalinity, and alkalinity (Olsen et al., 2016), and (3) BGC-Argo float profiles of $NO_3$ and $O_2$ (Drucker & Riser, 2016; Riser et al., 2018). Since BGC-Argo DIC and alkalinity are derived from an empirical relation between pH
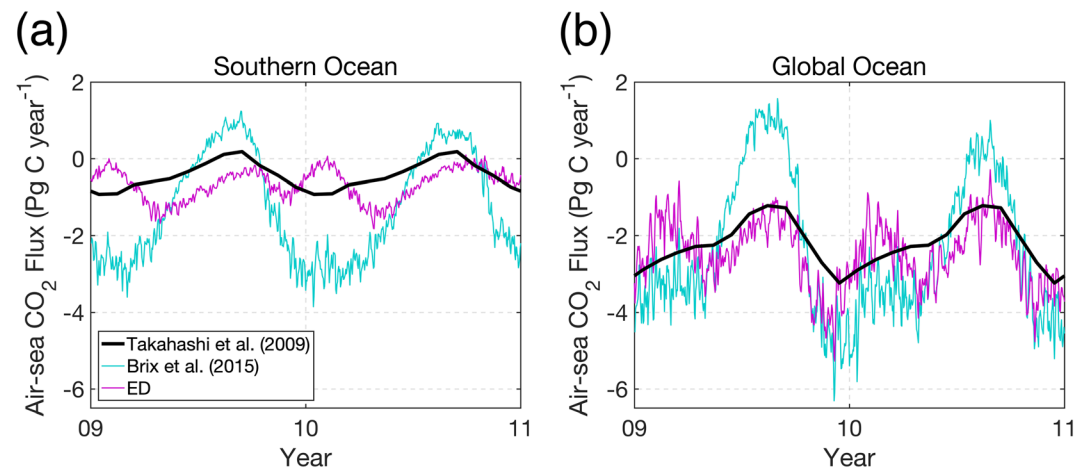
**Figure 1.** Comparison of daily (a) Southern Ocean and (b) global ocean integrated air-sea $CO_2$ flux during 2009–2011 from the monthly climatology of Takahashi et al. (2009) (black thick line), Brix et al. (2015) optimized simulation (thin cyan line), and the ED simulation presented in this paper (magenta thin line). The Southern Ocean is defined as all wet grid cells south of 45°S.

and salinity and therefore have larger uncertainty compared to GLODAPv2 observations, we verified that inclusion or exclusion of these observations had negligible impact (<1% change to globally integrated air-sea $CO_2$ fluxes) before including them as data constraints.

In addition to a better fit to the above observations, we sought to fix three serious biogeochemical issues with the pilot study of Brix et al. (2015):

(I1) Southern Ocean air-sea $CO_2$ flux synoptic variability that was strongly exaggerated compared to flask observations (see bottom panels of Figure 5 in Ott et al., 2015).

(I2) Southern Ocean air-sea $CO_2$ flux seasonal cycle that was much larger (Figure 1(a), cyan thin line) than the monthly climatology of Takahashi et al. (2009) (Figure 1a, black thick line).

(I3) The global-mean air-sea $CO_2$ flux was arbitrarily constrained to be approximately 2.4 Pg C year$^{-1}$ during the Green's function optimization (Figure 1b, cyan thin line).

To fix issues I1–I3 and improve the model's fit to the global biogeochemical observations, we used a Green's function approach to adjust biogeochemical initial conditions and six model parameters. Green's functions consist of forward model sensitivity experiments that express the linearized response of a forward model integration to perturbations of initial/boundary conditions and model parameters. We note that the Green's function approach (used to adjust the biogeochemistry) and the adjoint method (used to adjust the ocean physics) are both linearized least squares minimization approaches. The main difference is that Green's function approach can, in practice, only be applied to a small number of control variables (Menemenlis et al., 2005). Given the computational cost of each model sensitivity experiment, we are not able to conduct an exhaustive exploration of model parameter space. Instead, we selected a small number of sensitivity experiments that, in the authors' collective expertise, seemed the most likely to reduce model-data differences.

The first guess unadjusted experiment (Table 1, Experiment #1) used the optimized biogeochemical initial conditions and model parameters of Brix et al. (2015) but applied to the ECCO LLC270 ocean circulation estimate. To reduce the large initial drift in the model's biogeochemistry, Experiment #2 repeated the 1992–2017 model integration but starting from the 1996 biogeochemical conditions of Experiment #1. Because the Brix et al. (2015) DIC and alkalinity initial conditions were biased low compared to GLODAPv2 observations (Olsen et al., 2016), Experiments #3–5 attempted various combinations of initial conditions with increased DIC and alkalinity and GLODAPv2 climatological initial conditions. Experiment #6 is an interim optimization (supporting information Table S1). Experiments #7–11 are additional initial condition sensitivity experiments whose primary objective was to further reduce model drift in the equatorial Pacific.

**Table 1**
*Summary of the Biogeochemical Green's Functions Optimization*

| A | B | C | D | E | F |
|---|---|---|---|---|---|
| | | | Optimized linear combination | Cost relative to Brix et al. (%) | |
| # | Initial condition experiments | | | All observations | Surface ocean $pCO_2$ |
| 1 | Initial conditions from Brix et al. (2015) | | | 100 | 100 |
| 2 | Initial conditions from a 4-year spin up of #1 | | 0.0032 | 100.42 | 97.27 |
| 3 | Initial conditions from #2 with DIC/alkalinity + 150 mmol m$^{-3}$ | | 0.0012 | 68.98 | 103.16 |
| 4 | Initial conditions from #2 with GLODAPv2 DIC/alkalinity | | −0.1278 | 37.64 | 100.27 |
| 5 | Initial conditions from #2 with GLODAPv2 | | 0.1233 | 33.08 | 95.39 |
| 6 | Interim optimization | | −0.6314 | 32.03 | 95.48 |
| 7 | Initial conditions from a 4-year spin up of #6 | | 0.24415 | 33.29 | 92.84 |
| 8 | Initial conditions from a 6-year spin up of #6 | | −0.0218 | 34.10 | 94.26 |
| 9 | Initial DIC/alkalinity conditions from (#7 + #8) /2 | | 0.5702 | 31.99 | 95.18 |
| 10 | Initial DIC/alkalinity conditions from #8 | | −0.6618 | 32.55 | 95.13 |
| 11 | Initial DIC in equatorial Pacific from #8 | | 1.5008 | 31.84 | 94.42 |
| # | Parameter sensitivity experiments | Brix et al. value | Optimized value | All observations | Surface $pCO_2$ |
| 12 | Iron dust solubility − 20% | 1 | 0.9283 | 102.09 | 100.71 |
| 13 | Iron scavenging rate × 5 | 3 | 10.411 | 98.77 | 95.26 |
| 14 | Small phytoplankton growth rate + 10% | 0.7 | 0.6609 | 99.70 | 98.69 |
| 15 | Large phytoplankton growth rate + 10% | 0.4 | 0.4314 | 99.70 | 99.37 |
| 16 | Diatom palatability + 0.1 | 0.85 | 0.8300 | 99.54 | 97.31 |
| 17 | PIC/POC ratio + 20% | 0.04 | 0.04245 | 99.69 | 97.47 |
| 18 | Optimized simulation | | | 31.90 | 94.00 |

*Note.* The Brix et al. (2015) "first guess" simulation that we started with is listed as Experiment #1. The optimized ED simulation (Experiment #18) uses (1) biogeochemical initial conditions that are a linear combination of Experiments #2–11 according to the coefficients listed in column D and (2) optimized model parameters listed in rows #12–17 of column D. The cost relative to the Brix et al. simulation is reported in columns E (for all observations) and F (for surface ocean $pCO_2$ observations). PIC = particulate inorganic carbon; POC = particulate organic carbon.

Since iron is an important limiting micronutrient in several key areas of the ocean (Martin & Fitzwater, 1988), Experiments #12–13 perturbed iron dust solubility, which is poorly known, and iron scavenging rate, which can vary by orders of magnitude (e.g., Parekh et al., 2005). We also perturbed phytoplankton growth rates parameters (Experiments #14–15), which are critical for the amount of carbon taken up by these organisms. Since diatoms are one of the key components of the Southern Ocean marine food web, Experiment #16 altered their palatability to grazers in order to explore how some top-down control on the system impacts air-sea $CO_2$ fluxes. Finally, we also altered the amount of particulate inorganic carbon produced per particulate organic carbon (Experiment #17); this value likely varies significantly over the global ocean (Sarmiento et al., 2002). Because particulate inorganic carbon production and dissolution have a large impact on alkalinity, which strongly influences $pCO_2$ concentrations, this parameter is a good candidate for optimization.

Using the above sensitivity experiments and the Green's function approach described in Menemenlis et al. (2005), we minimized a quadratic "cost" function of weighted model-data differences to obtain optimized biogeochemical initial conditions and model parameters. Table 1 summarizes some results from this optimization. Experiments #2–11 pertain to initial condition sensitivity experiments, while Experiments #12–17 pertain to biogeochemical model parameters. The optimized biogeochemical initial conditions are constructed as a linear combination of Experiments #2–11, according to the coefficients listed under column D (which sum to one). For Experiments #12–17, columns C–D show initial and optimized values for each adjusted parameter. The ED simulation described in this paper (Experiment #18 in Table 1) uses the optimized biogeochemical initial conditions and the optimized biogeochemical parameters of Table 1. Therefore, ED represents a well-tuned biogeochemical model simulation driven by adjoint method-constrained ocean physics provided by the ECCO project.

Figure 2 shows a scatterplot of observations versus simulations before and after the biogeochemical adjustments. The cost function reduction of ED (Experiment #18) relative to the first guess simulation based on
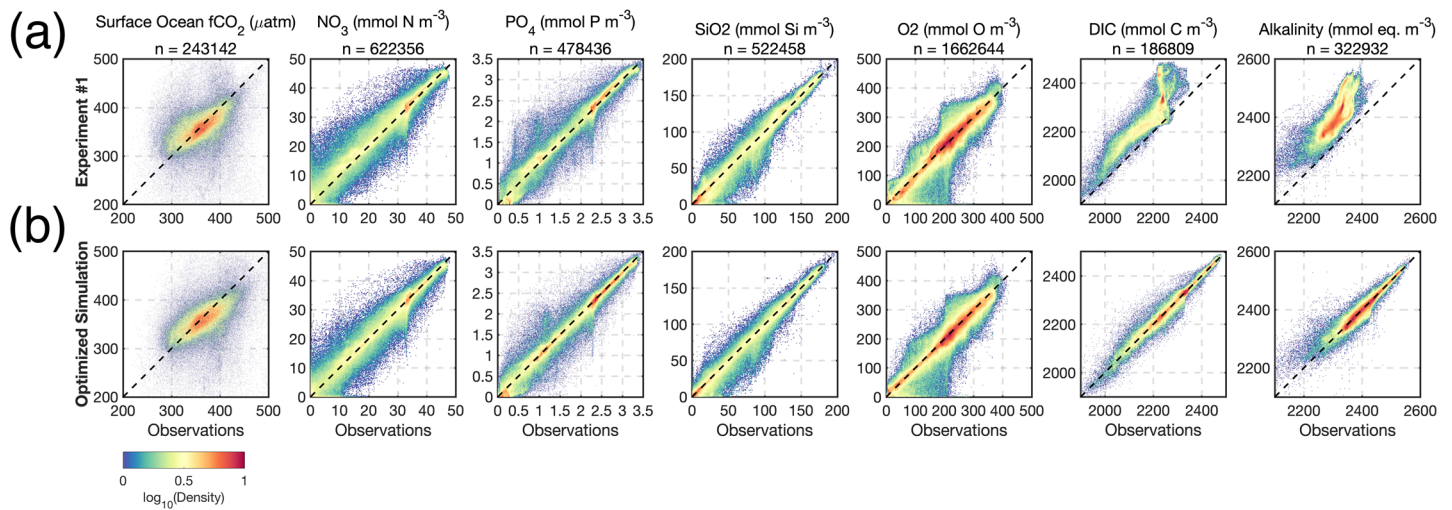
**Figure 2.** Comparison of observed and modeled surface ocean fugacity ($f$CO$_2$) and biogeochemical profiles for the (a) Brix et al. (2015) first guess simulation (Experiment #1, table 1) and (b) ED optimized simulation. The $x$ axis shows observations and $y$ axis shows the corresponding model value at the same space-time location. Colors represent the density of observation-model pairs in log scale; the total number of observations is shown above each panel.

Brix et al. (2015) (Experiment #1) is 6%, 36%, 32%, 26%, 19%, 95%, and 96%, respectively, for surface ocean $f$CO$_2$, NO$_3$, PO$_4$, SiO$_2$, O$_2$, DIC, and alkalinity. Being at the surface, $f$CO$_2$ has elevated synoptic variability, and therefore, the cost function reduction is smaller than the other full-depth variables; the largest cost function decrease is for DIC and alkalinity. The overall biogeochemical cost function reduction of ED (Experiment #18) relative to the first guess simulation based on Brix et al. (2015) (Experiment #1) is ~68% (Column F in Table 1).

As is discussed in Menemenlis et al. (2005), the Green's function approach permits offline parameter sensitivity exploration as well as the exploration of different cost functions. For example, columns E and F of Table 1 indicate the importance of each sensitivity experiment in fitting the biogeochemical observations. Specifically, each row of columns F and G display the cost of the various sensitivity experiments relative to the Brix et al. (2015) initial conditions and parameter values (Experiment #1). For the initial condition experiments and optimized simulation (#2–11 and #18), we directly report the relative cost of each individual simulation. For the parameter sensitivity experiments (#12–17), we report the expected cost of a simulation that would start with the Brix et al. (2015) initial conditions but use the optimized value of each parameter, one at a time, while the remaining parameters retain the Brix et al. (2015) values. The expected cost for the optimized parameters is estimated based on the model sensitivity experiments under the assumption that the model response to parameter perturbations is linear. We have verified that the assumption of a linear response is approximately satisfied by comparing the expected cost of the optimized linear combination, 30.85% of Experiment #1 cost, to the actual relative cost of the optimized simulation, 31.90% of Experiment #1 (Column E, Experiment #18 in Table 1).

For the full-depth set of observations (column E), most of the cost function reduction comes from the GLODAPv2 initial conditions (Experiment #5). This is because over the 26-year integration period, there is little change to biogeochemical properties in the deep ocean. If we focus on upper ocean observations only, for example, if we only include surface ocean $p$CO$_2$ observations in the cost function (column G), the most significant cost reduction results from sensitivity experiments that reduce solution drift (Experiments #7–11) and from the adjustment of iron scavenging rate (Experiment #13). A different method to establish the contribution of each parameter to the optimized solution is to remove each parameter from the optimization, one at a time, as is done in Table 3 of Menemenlis et al. (2005). Using this method, the most important parameter for improving surface ocean $p$CO$_2$ relative to Brix et al. (2015) is the large phytoplankton growth rate, which contributes 39% cost reduction, followed by iron scavenging rate, iron dust solubility, and small phytoplankton growth rate, which contribute, respectively, 22%, 15%, and 11% cost reduction.

Note that contrary to Brix et al. (2015), the present ED solution uses pure observations as constraints and does not rely on an additional arbitrary constraint for the global ocean $CO_2$ sink. The initial condition biases in DIC and alkalinity turned out to be the major causes for all three (I1–I3) issues in the older ED simulation. As shown in Brix et al. (2015), the Green's function approach reduces both bias and drift for biogeochemistry, similar to the adjoint-based method for the physics. We further remove any residual "large" drift by discarding the first 2 years (1992–1994) of the ED simulation in our analysis, where large is defined relative to the interpolation-based estimates of the global ocean $CO_2$ sink. This residual model drift occurs primarily in the Southern Ocean.

### 2.5. Comparison With Interpolation-Based Products

To illustrate the performance of ED and its ability to reproduce air-sea $CO_2$ flux spatiotemporal variability, we compared model output with three interpolation-based surface ocean $pCO_2$ and air-sea $CO_2$ flux products:

1. The 4° × 5° monthly gridded climatological product of Takahashi et al. (2009), which uses statistical interpolation combined with an advection-diffusion equation and is referenced to the year 2000.
2. The 4° × 5° daily gridded product of Rödenbeck et al. (2013), which spatiotemporally interpolates surface ocean $pCO_2$ observations while remaining compatible with mixed-layer DIC dynamics. Surface ocean pCO2 and air-sea $CO_2$ fluxes are first linked to each other, and to the spatiotemporal field of internal ocean carbon sources/sinks, through parameterizations of air-sea gas exchange, solubility, and carbonate chemistry, as well as a budget equation for the mixed layer DIC content. The internal ocean carbon sources/sinks are then adjusted to optimally fit the surface ocean $pCO_2$ field to the observations. Spatiotemporal interpolation is achieved by enforcing source/sink adjustments to be smooth; temporal interpolation is overlaid by the inherent relaxation timescales of the mixed layer DIC budget. Process parameterizations are driven by SST, wind speed, mixed layer depth climatology, alkalinity climatology, and some auxiliary variables. However, this external variability only determines features not constrained by surface ocean $pCO_2$ observations (e.g., day-to-day variations or variability in data-sparse regions/time periods), while the estimated surface ocean $pCO_2$ field in well-constrained regions/time periods is determined by the observed signal (i.e., there is no regression against environmental drivers). We use version oc_v1.6 of this product, extended in time to December 2017 based on SOCATv6 (Bakker et al., 2016).
3. The 1° × 1° monthly gridded, smoothed product of Landschützer et al. (2013), which uses an observation-based, self-organizing map feed forward neural network (SOM-FFN). For the purpose of this work, we extend this product in time to December 2017 and adjusted the Arctic Ocean mask to be more consistent with the products of Takahashi et al. (2009) and Rödenbeck et al. (2013). The two-step SOM-FFN method first clusters the ocean into biogeochemical regions and then establishes relationships between SOCATv6 surface ocean $pCO_2$ observations and environmental drivers (i.e., SST and salinity, mixed layer depth, satellite-based chlorophyll $a$, and atmospheric $pCO_2$). More details regarding the SOM-FFN method and its evaluation can be found in Landschützer et al. (2014, 2016, 2018).

These interpolation-based products, hereby referred to in this paper as Tak09, Röd13, and Land13, respectively, are interpolated and land masked onto the ED model grid using nearest-neighbor interpolation; air-sea $CO_2$ fluxes are conserved during the interpolation.

Additionally, we account for the land-ocean river runoff loop of $CO_2$ in the interpolation-based products by subtracting an area-weighted runoff contribution from air-sea $CO_2$ flux in each wet grid cell, as done in Le Quéré et al. (2018) and Friedlingstein et al. (2019). Globally integrated, the runoff contribution to the global ocean $CO_2$ sink is 0.78 Pg C year$^{-1}$ (Resplandy et al., 2018).

Statistically based interpolation methods, such as Tak09 and Röd13, are typically dominated by surface ocean $pCO_2$ observations and remain fairly independent of environmental driver data sets (e.g., SST, mixed layer depth, and chlorophyll $a$) and choice of process parameterizations. However, time-space sampling biases, particularly in data-sparse regions, can lead to the seasonal exclusion of air-sea $CO_2$ flux features and the creation of spurious artifacts. Regression-based interpolation methods such as Land13 allow for more complete space-time coverage by constructing nonlinear models between surface ocean $pCO_2$ and a suite of environmental drivers observed with more complete coverage. However, this approach can only reproduce modes of variability that are contained in the chosen environmental drivers. By comparison,

ED represents dynamical interpolation, where the ocean physics and many of the biogeochemical processes that drive variability in surface ocean $p\text{CO}_2$ are explicitly resolved. While ED contains inherent model errors, our solution is constrained by both the observed ocean circulation (adjoint-based ECCO LLC270) and biogeochemistry (low-dimensional Green's function optimization).

### 2.6. Biomes

We compute area-weighted mean surface ocean $p\text{CO}_2$ and spatially integrated air-sea $\text{CO}_2$ flux in the context of the time-independent $1° \times 1°$ open-ocean biomes described in Fay and McKinley (2014) (Figure A1 in Appendix A). The 17 biomes are determined from coherence between SST, spring and summer chlorophyll $a$, sea ice fraction, and maximum mixed layer depth and therefore provide a more robust estimate of biogeochemical ocean regions compared to rectangular boundaries (Fay & McKinley, 2014). All biomes are interpolated onto the ED model grid using nearest-neighbor interpolation.

### 2.7. Trend Analysis

In order to identify statistically significant trends in global ocean and biome-scale air-sea $\text{CO}_2$ flux, we perform a two-tailed Mann-Kendall test (Kendall, 1975; Mann, 1945), which is commonly used to detect monotonic trends in environmental data (Yue et al., 2002). Additionally, we modify this method to account for autocorrelation in the time series (Hamed & Rao, 1998). Trends are computed using a Theil-Sen linear regression (Gilbert, 1987) on annual mean air-sea $\text{CO}_2$ fluxes from 1995 to 2017; trend significance is evaluated at the 95% confidence level.

## 3. Results

### 3.1. Climatological Evaluation (1995–2017)

ED (which refers to the optimized simulation for the remainder of the paper) generally reproduces the time-mean large-scale spatial patterns of elevated surface ocean $p\text{CO}_2$ and outgassing in the equatorial regions and high-latitude uptake shown in all interpolation-based products (Figures 3 and 4). Additionally, the ED solution covers the complete Arctic domain and includes coastal regions (Figures 3a and 4a). On the regional scale, the higher-resolution ED solution exhibits more complex spatial patterns of outgassing in the Subtropical Pacific and Atlantic Oceans (Figure 4a) compared to the interpolation-based products (Figures 4b–4d). Here ED produces outgassing patches that extend 100 s of km offshore of coastal upwelling zones (e.g., Western North America, Central and South America, and northwest Africa), with reduced outgassing further offshore and near-equilibrium conditions in the convergence zones of the subtropical gyres. These outgassing features are weak or absent in the interpolation-based products, particularly in the South Pacific Ocean where surface ocean $p\text{CO}_2$ measurements are limited. We also note that ED and Land13 partially resolve the fine-scale coastal outgassing features located offshore of western Central America (Figures 4a and 4d). In the tropical Indian Ocean, particularly along the Arabian and Somalian coasts, ED exhibits weaker outgassing (maximum of ~1.7 mol C $\text{m}^{-2}$ $\text{year}^{-1}$) compared to the interpolation-based products (Land13 maximum of ~3.3 mol C $\text{m}^{-2}$ $\text{year}^{-1}$).

ED does not produce the strong outgassing patch southeast of the Bering Sea that is shown in the interpolation-based products (Figure 4), despite this region being data rich for surface ocean $p\text{CO}_2$ and biogeochemical profiles. Here ED results in a smaller patch of increased surface ocean $p\text{CO}_2$ (maximum of ~384 μatm) that is shifted westward (Figure 3a), with air-sea $\text{CO}_2$ fluxes characterized by weak uptake or near-equilibrium conditions (Figure 4a). Additionally, Southern Ocean outgassing in ED is shifted to higher latitudes (primarily south of 60°S) compared to interpolation-based products and is generally constrained along the periphery of Antarctica, where elevated surface ocean $p\text{CO}_2$ is present (Figure 3a). This is primarily due to the suppression of air-sea gas exchange by winter sea ice cover, followed by outgassing during periods of sea ice melt and open water. In the Arctic Ocean, ED has the highest surface ocean $p\text{CO}_2$ concentrations in the Canadian Basin (Figure 3a), with weak outgassing throughout the region (Figure 4a).

Time-mean uptake is generally stronger in ED compared to the interpolation-based products, particularly in the Southern Ocean and high-latitude Pacific and Atlantic Oceans (Figure 4). Additionally, ED produces stronger uptake along many of the western boundary currents and their respective extensions (e.g., the
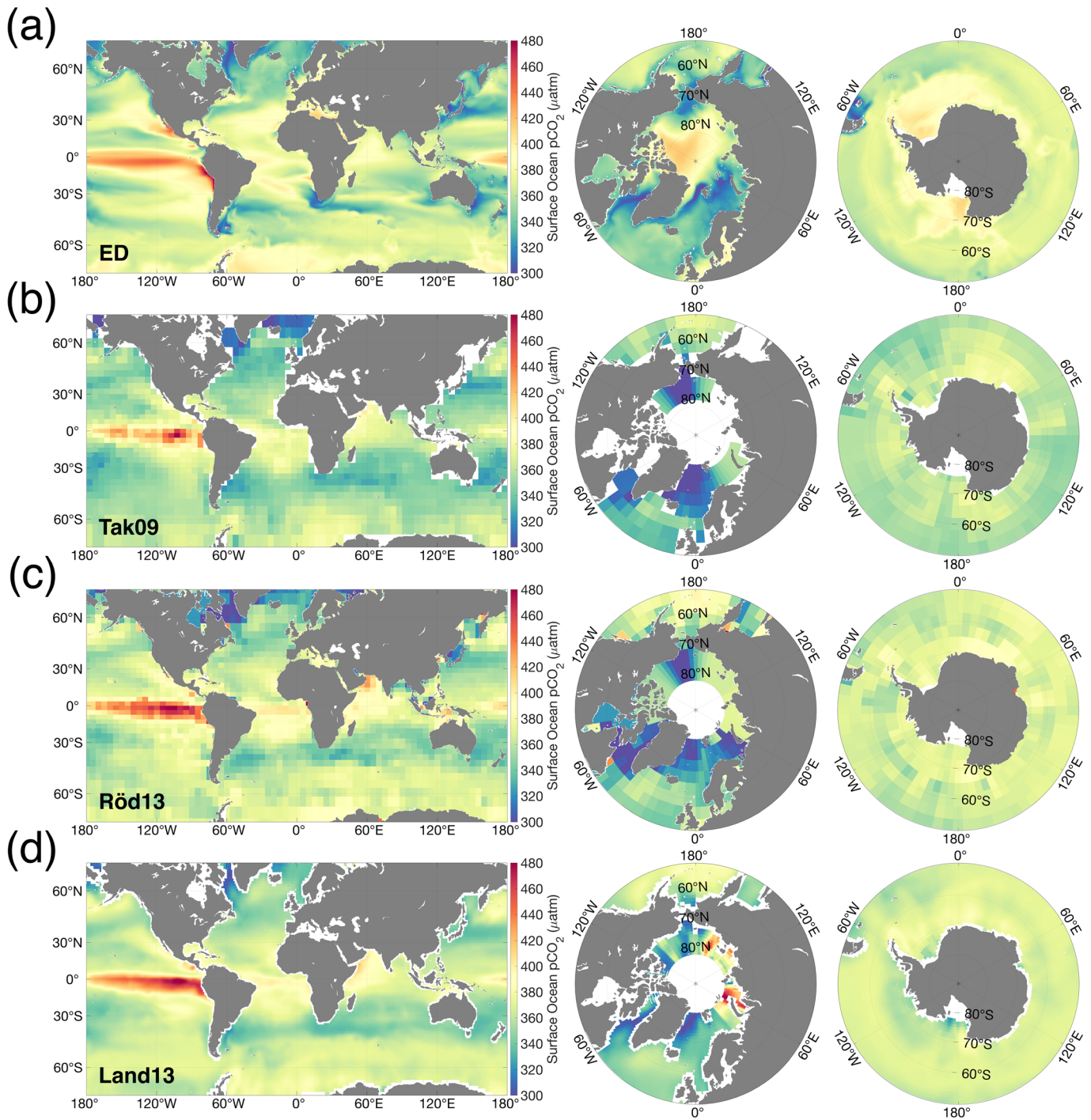
**Figure 3.** Long-term mean surface ocean $p\mathrm{CO}_2$ for (a) ED, (b) Tak09, (c) Röd13, and (d) Land13. Tak09 is referenced to the year 2000; ED, Röd13, and Land13 are time averaged from January 1995 to December 2017. Regions north of 80°N in Tak09, Röd13, and Land13 are excluded due to data sparsity.

Gulf Stream, Kuroshio, and East/West Greenland Currents). Zonally averaged air-sea $\mathrm{CO}_2$ fluxes highlight the pole-to-pole patterns of ocean outgassing and uptake (Figure 5). Compared to the interpolation-based products, ED air-sea $\mathrm{CO}_2$ fluxes show enhanced zonal variability (Figure 5, blue line in top panel), particularly between 15–45°S and 30–45°N. Additionally, ED results in stronger uptake between 60–45°S and 35–65°N (Figure 5, bottom panel). Near the equator (7.5°S–7.5°N), the zonally averaged ED air-sea
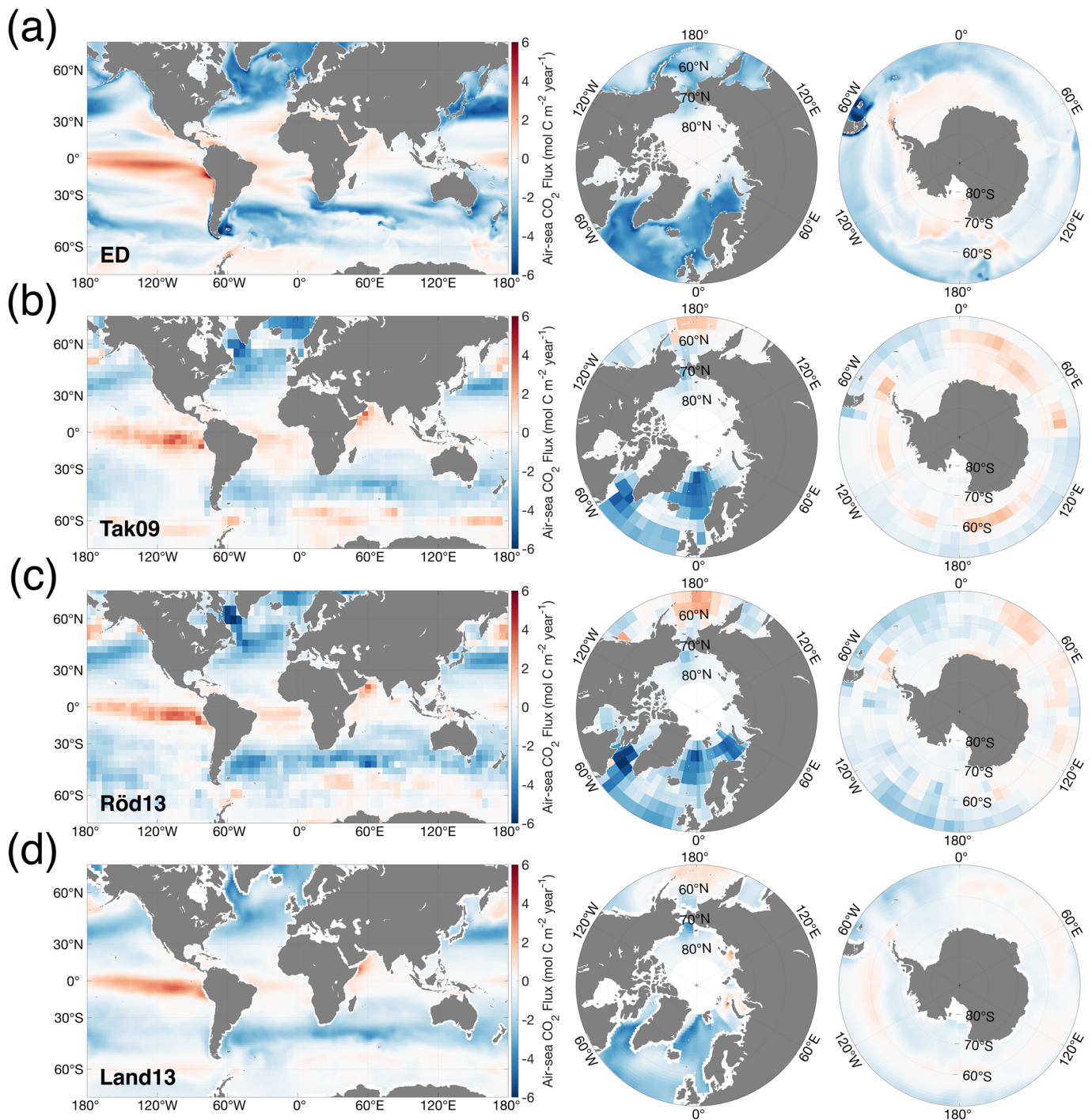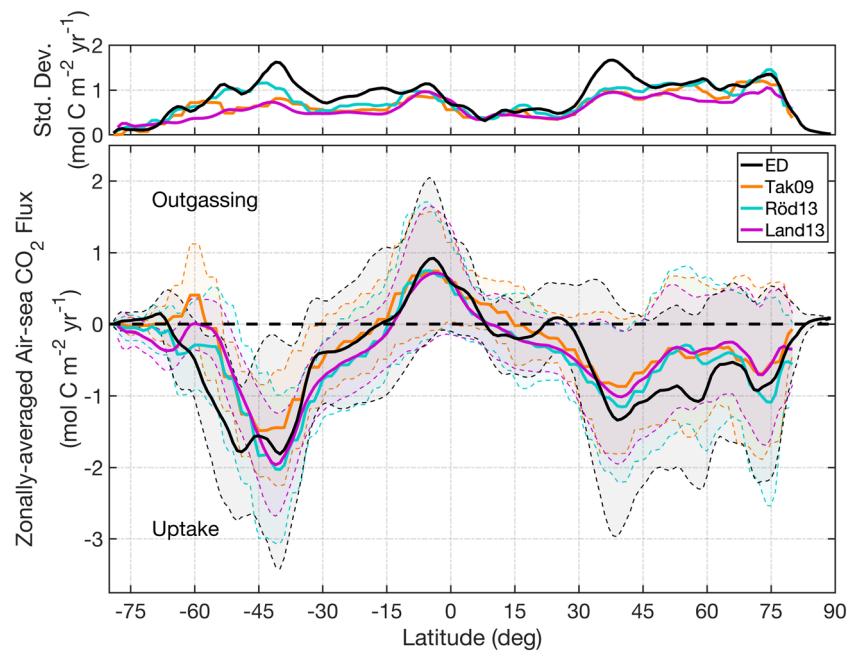
**Figure 4.** Long-term mean global air-sea $CO_2$ fluxes for (a) ED, (b) Tak09, (c) Röd13, and (d) Land13. Positive values represent outgassing (red); negative values are uptake (blue). Tak09 is referenced to the year 2000; ED, Röd13, and Land13 are time averaged from January 1995 to December 2017. Regions north of 80°N in Tak09, Röd13, and Land13 are excluded due to data sparsity.

$CO_2$ flux magnitude and variability agrees well with the interpolation-based products (Figure 5); here ED and all interpolation-based products show peak outgassing at ~4°S.

### 3.2. Biome-Scale Seasonality

We now zoom into the biome scale and examine the seasonal cycle of air-sea $CO_2$ flux (Figure 6) and surface ocean $p$CO$_2$ (Figure A2). For a map of the biomes used in this section see Figure A1. Additionally, monthly

**Figure 5.** Long-term mean air-sea $CO_2$ flux for ED (black), Tak09 (orange), Röd13 (cyan), and Land13 (magenta) as a function of latitude. Air-sea $CO_2$ fluxes are zonally averaged in 1° bins. Positive values represent outgassing, and negative values are uptake; black horizontal dashed line shows zero flux. Top panel and shaded error bars in bottom panel show zonal variability (one standard deviation). Tak09 is referenced to the year 2000; ED, Röd13, and Land13 are time-averaged from January 1995 to December 2017. Regions north of 80°N in Tak09, Röd13, and Land13 are excluded due to data sparsity.

climatological fields of surface ocean $p$CO$_2$ and air-sea $CO_2$ flux for ED and the interpolation-based products are shown in supporting information Figures S6 and S7, respectively.

In terms of the amplitude and phase of the seasonal cycle, we find the closest agreement between ED and the interpolation-based products in the Pacific, Atlantic, and Indian subtropical permanently stratified biomes (STPS, biomes 4, 7, 11, 13, and 14) and seasonally stratified biomes (STSS, biomes 3 and 10). For all Pacific and Atlantic STPS and STSS biomes, ED produces air-sea $CO_2$ flux and surface ocean $p$CO$_2$ seasonal amplitudes that are larger than the interpolation-based products (Figure A2), while Röd13 has the strongest seasonality of all interpolation-based products. In the equatorial biomes (EQU, biomes 5, 6, and 12), which are strongly influenced by interannual variability driven by El Niño–Southern Oscillation (ENSO) events, we find limited seasonality and poor matchup between the individual interpolation-based products and ED. In particular, ED shows a strong decrease in AEQU (biome 12) $CO_2$ outgassing during spring-summer, with a transition to uptake during August; this feature is coincident with increased phytoplankton blooms offshore of West Africa (not shown).

At higher latitudes in the Pacific and Atlantic subpolar seasonally stratified biomes (SPSS, biomes 2 and 9), ED produces weak outgassing and near-equilibrium conditions in, respectively, the NP SPSS and NA SPSS biomes during summer. The NA SPSS summer decrease in uptake (Figure 6, biome 2) is primarily driven by strong outgassing on the Scotian Shelf, which is less pronounced in the interpolation-based products (supporting information Figure S2). During fall-winter, ED results in stronger uptake compared to the interpolation-based products. For these biomes, ED surface ocean $p$CO$_2$ is generally out of phase with the interpolation-based products (Figure A2, biomes 2 and 9). In the Southern Ocean, ED results in a larger air-sea $CO_2$ flux seasonal amplitude of 1.25 Pg C year$^{-1}$ in SO STSS (biome 15), compared to 0.19, 0.13, and 0.15 Pg C year$^{-1}$ in Tak09, Röd13, and Land13, respectively. This difference is highlighted by the surface ocean $p$CO$_2$ seasonal amplitude; here the ED amplitude (~40 µatm) is a factor of ~3 larger than Tak09 and Land13 and a factor ~8 larger than Röd13 (Figure A2, biome 15). Further south in the Southern Ocean SPSS biome (biome 16), the ED seasonal amplitude is in closer agreement with the interpolation-based products;
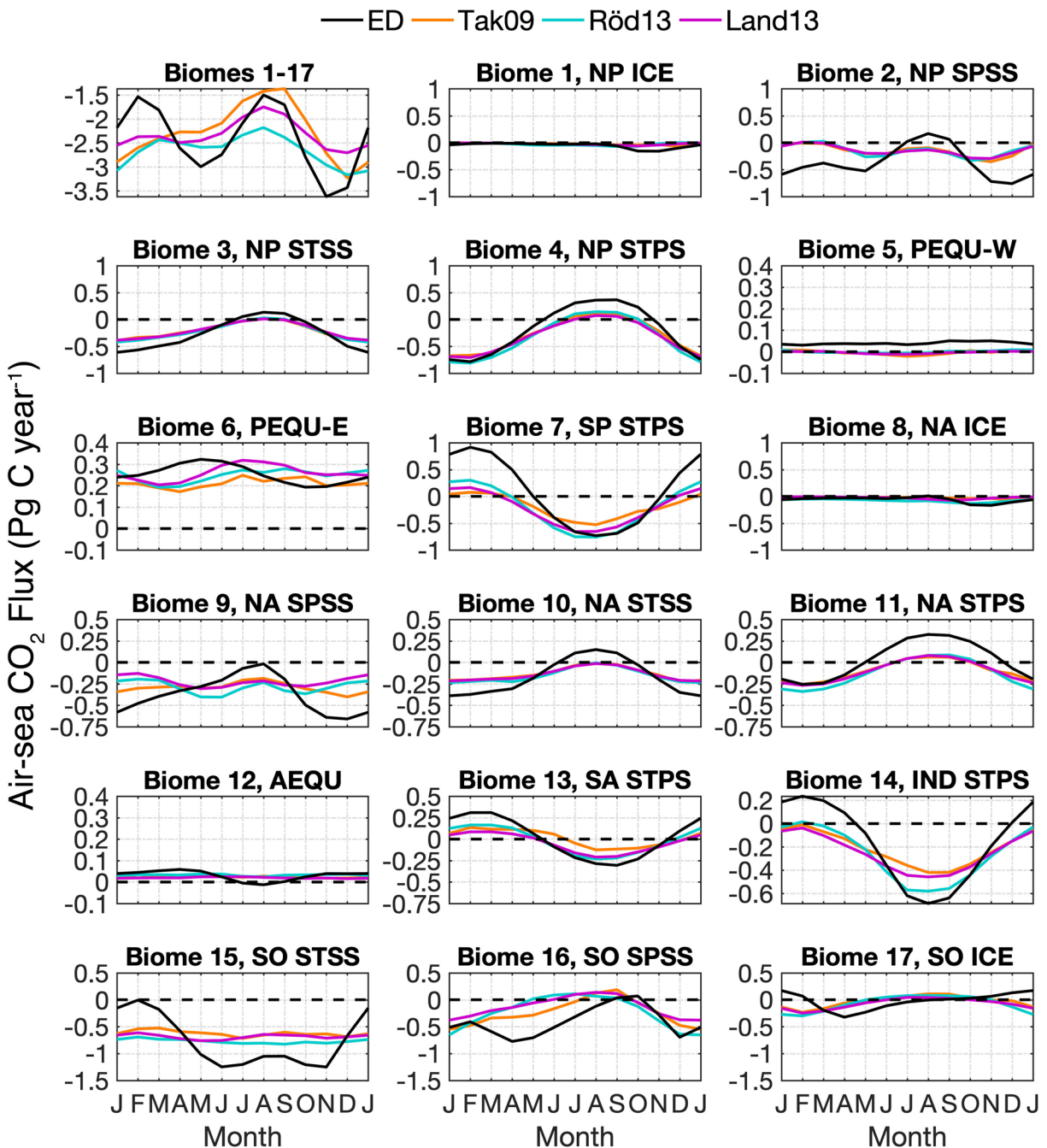
**Figure 6.** Seasonal cycle of air-sea $CO_2$ flux for ED (black), Tak09 (orange), Röd13 (cyan), and Land13 (magenta) in each biome. Air-sea $CO_2$ fluxes are time-averaged for each month (January 1995 to December 2017) and spatially integrated across each biome. Similar $y$ axis scales are used for each individual ocean basin; horizontal black dashed lines show zero flux.

however, ED results in stronger uptake during February–September. For biomes that are influenced by sea ice cover year-round (ICE biomes 1, 8, and 17), ED and the interpolation-based products diverge in both amplitude and phase.

### 3.3. Biome-Scale Interannual to Multidecadal Variability (1995–2017)

Next, we evaluate time series of air-sea $CO_2$ flux and surface ocean $pCO_2$ for ED, Röd13, and Land13 in each biome (Figures 7 and A3). Additionally, time series of surface ocean $fCO_2$ for ED and SOCATv5 and the
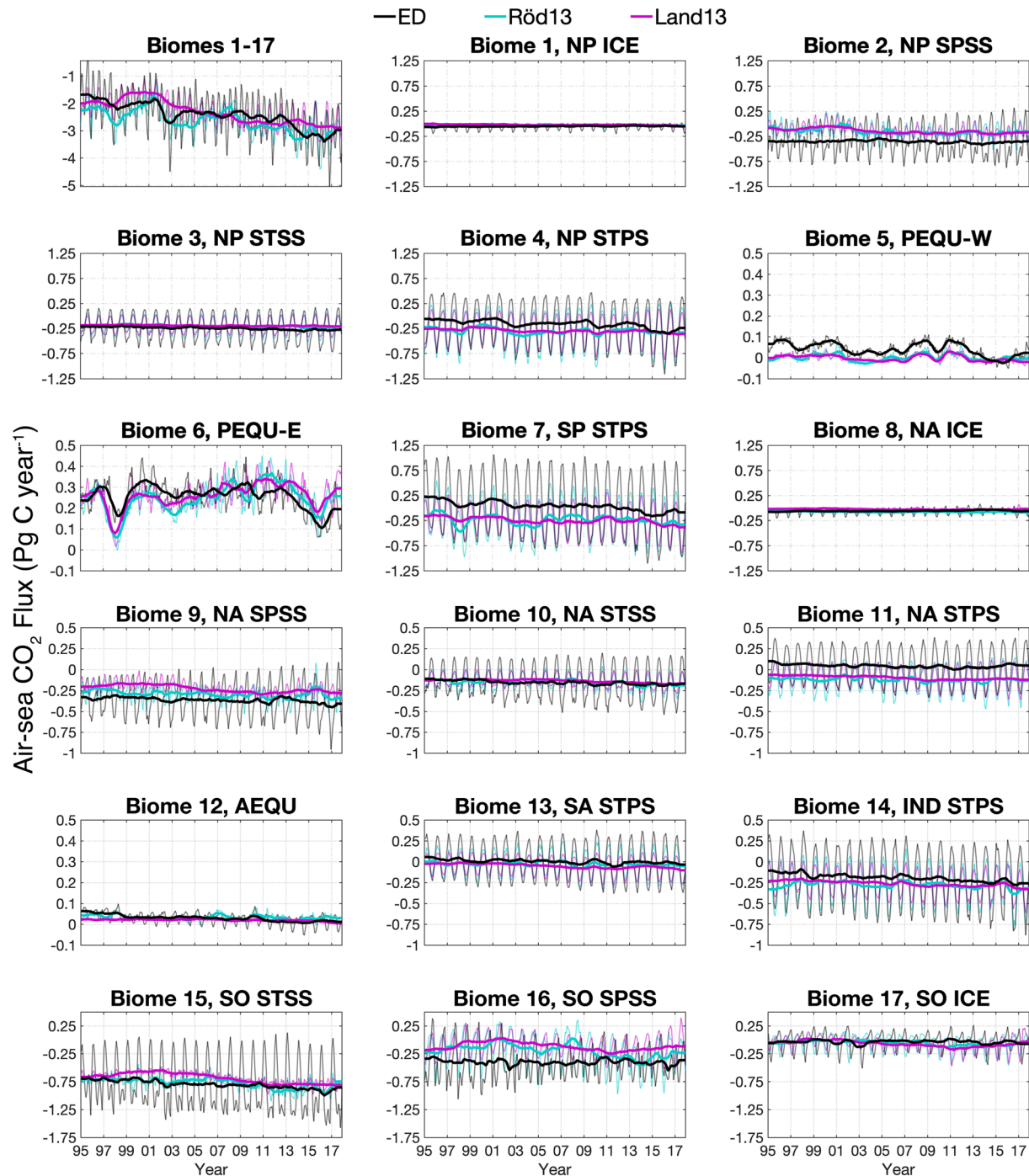
**Figure 7.** Air-sea $CO_2$ flux time series for ED (black), Röd13 (cyan), and Land13 (magenta) in each biome. Air-sea $CO_2$ fluxes are spatially integrated across their respective biomes. Positive values represent outgassing; negative values are uptake. Thin lines show monthly values, and thick lines show interannual variability (12-month running mean). Similar *y* axis scales are used for each individual ocean basin.

corresponding number of observed $f$CO$_2$ points per month are shown in, respectively, Figures A4 and A5. Integrated across all biomes, ED results in a time-mean uptake of $-2.42$ Pg C year$^{-1}$, which lies within the Röd13 and Land13 time-mean estimates of $-2.63$ and $-2.32$ Pg C year$^{-1}$, respectively (Figure 7, biomes 1–17). Here ED and Röd13 show increased interannual variability in air-sea $CO_2$ fluxes compared to the spatially less heterogeneous Land13 product. We find that ED generally has higher mean surface

ocean $pCO_2$ and a stronger seasonal cycle compared to Röd13 and Land13 (Figure A3, biomes 1–17). For all biomes, ED, Röd13, and Land13 all exhibit statistically significant air-sea $CO_2$ flux trends over the period examined (supporting information Table S2).

Similar to the seasonal results, we find good agreement in interannual air-sea $CO_2$ flux and surface ocean $pCO_2$ magnitude and trend between ED and the interpolation-based products in the Pacific, Atlantic, and Indian STSS and STPS biomes (Figures 7 and A3, biomes 3, 4, 7, 10, 11, 13, and 14). For these biomes, the largest differences between ED and the interpolation-based products occur in NA STSS (biome 11), where the larger ED surface ocean $pCO_2$ seasonal amplitude biases air-sea $CO_2$ fluxes toward $CO_2$ outgassing. ED and Land13 show statistically significant trends in air-sea $CO_2$ fluxes for all Pacific, Atlantic, and Indian STSS and STPS biomes, with Röd13 only exhibiting a statistically significant trend in NP STSS (biome 3).

Equatorial biomes have the largest interannual variability in air-sea $CO_2$ flux and surface ocean $pCO_2$ (biomes 5, 6, and 12), with temporal variability in the equatorial Pacific biomes (PEQU) strongly modulated by ENSO events (biomes 5 and 6). ED shows considerable skill in reproducing the interannual variability shown in Röd13 and Land13, particularly in PEQU-E (biome 6). Additionally, we find that ED produces a stronger reduction in PEQU outgassing compared to the interpolation-based products during the 2015–2016 ENSO, which may be due to lower surface ocean $pCO_2$ during this time period (Figure A3). Interestingly, only ED has statistically significant air-sea $CO_2$ flux trends in PEQU-W and PEQU-E, while both ED and Land13 obtain statistical significance in AEQU (biome 12).

For NP and NA SPSS (biomes 2 and 9), ED results in stronger uptake (factor of ~3 and ~1.3 larger in NP SPSS and NA SPSS, respectively) compared to Röd13 and Land13. In the Southern Ocean STSS (biome 15), ED and Röd13 have comparable statistically significant trends ($-0.0091$ and $-0.0088$ Pg C year$^{-2}$, respectively), while Land13 has a larger significant trend ($-0.0128$ Pg C year$^{-2}$) (supporting information Table S2). We note that Land13 shows decreasing $CO_2$ uptake in SO STSS during 1996–2002, followed by an increase until 2011; this weakening and reinvigoration event is not captured by ED and Röd13 in this biome. ED interannual variability in SO SPSS (biome 16) is more muted, with Röd13 having variable but increasing uptake during 2002–2014 and Land13 showing a similar temporal response to SO STSS. All air-sea $CO_2$ flux trends in SO STSS fail to reach statistical significance, with Röd13 having the smallest $p$ value (supporting information Table S2). Similar to the seasonal results, there is limited temporal coherence between ED and the interpolation-based products in NP, NA, and SO ICE (biomes 1, 8, and 17).

## 4. Discussion

While data-based reconstructions of the global ocean carbon sink have made major advances in recent years, OMBs continue to play an important role, especially since they allow for a process-based understanding of the ocean carbon sink. The ideal scenario, however, is a combination of these two methods through some form of data assimilation. While the physical oceanographic community has made great strides in the development of data assimilation systems (e.g., ECCO), the biogeochemical community has generally lagged behind. Therefore, the work presented in this paper represents an important technological step forward in ocean biogeochemical data assimilation since ED is the first global OBM model that (1) assimilates both physical and biogeochemical observations in a property-conserving manner (i.e., by adjusting model parameters and initial conditions, as opposed to nonconserving optimal interpolation and Kalman filter approaches) and (2) considers the time-varying nature of the ocean carbon sink over multidecadal timescales.

Using only a small number of model adjustments (biogeochemical initial conditions and six model parameters), ED produces air-sea $CO_2$ flux estimates that show broad-scale consistency with Tak09, Röd13, and Land13, particularly in the subtropical and equatorial biomes. The low dimensionality of this biogeochemical adjustment highlights the strength of the adjoint-based ECCO LLC270 ocean physics in reproducing observed trends in the ocean carbon sink (DeVries et al., 2017, 2019; McKinley et al., 2017). Compared to interpolation-based products, the higher-resolution ED simulation also allows for a better representation of fine-scale ocean features (e.g., boundary currents, fronts, and coastal regions), along with covering the complete Arctic Ocean.

**Table 2**
*Time-Averaged Global Ocean Air-Sea $CO_2$ Flux for ED, GCP 2019, Röd13, and Land13*

| Global ocean | Jan 1995–Dec 2000 | Jan 2000–Dec 2005 | Jan 2005–Dec 2010 | Jan 2010–Dec 2015 | Jan 2015–Dec 2017 | Jan 1995–Dec 2017 |
|---|---|---|---|---|---|---|
| ED | −1.89 ± 0.22 | −2.26 ± 0.34 | −2.43 ± 0.08 | −2.79 ± 0.31 | −3.29 ± 0.20 | −2.47 ± 0.50 |
| GCP 2019 | −1.96 ± 0.59 | −2.05 ± 0.68 | −2.29 ± 0.55 | −2.46 ± 0.60 | −2.62 ± 0.57 | −2.24 ± 0.76 |
| Röd13 | −2.39 ± 0.23 | −2.43 ± 0.49 | −2.52 ± 0.17 | −3.05 ± 0.18 | −3.09 ± 0.30 | −2.66 ± 0.41 |
| Land13 | −1.84 ± 0.18 | −1.84 ± 0.27 | −2.45 ± 0.16 | −2.68 ± 0.07 | −2.85 ± 0.07 | −2.29 ± 0.45 |

One problematic aspect of model-based biogeochemical estimates is bias and drift. It is possible to reduce drift at the expense of bias by spinning up a model toward equilibrium. Alternatively, it is possible to reduce bias at the expense of drift by forcing the model solution to be very close to the observations. Various ad hoc corrections have been devised to minimize the impact of bias and drift on model solutions (e.g., Sausen et al., 1988). The Global Carbon Project (GCP) corrects for model bias and drift by subtracting a time-dependent model bias calculated as a linear fit to the annual $CO_2$ flux from a control simulation carried out with constant, preindustrial atmospheric $CO_2$ concentration (Friedlingstein et al., 2019). Instead of ad hoc corrections, bias and drift reduction can be addressed as an optimization problem whereby model parameters and initial conditions are adjusted to simultaneously reduce model bias and drift relative to observations (e.g., Tziperman & Thacker, 1989).

As demonstrated in Brix et al. (2015), a Green's function optimization can be used to reduce bias and drift in a global ocean biogeochemistry model. Unlike the proof-of-concept ED model described in Brix et al. (2015), however, the simulation presented in this paper does not require an arbitrary constraint on global mean air-sea $CO_2$ flux in the optimization process. Supporting information Figure S8 compares air-sea $CO_2$ flux time series in the Fay and McKinley (2014) biomes, similar to Figure 7, except that we include the first 2 years (1992–1994) of the simulations during which there is larger drifts, as well as showing time series for the simulation based on the Brix et al. (2015) initial biogeochemical conditions and parameters (Experiment #1 in Table 1) and the interim optimization (Experiment #6). Relative to Experiments #1 and #6, the optimized Experiment #18 removes most of the initialization transients in the equatorial Pacific (Biomes 5 and 6), reduces the unreasonably large seasonal cycle in the SO SPSS (Biome 16), but does not remove the Southern Ocean initialization transients (Biomes 15–17).

For the 1995–2017 period, the ED time-mean global ocean $CO_2$ sink is −2.47 ± 0.50 Pg C year$^{-1}$, which lies within the uncertainty of the GCP estimate of −2.24 ± 0.76 Pg C year$^{-1}$ over the same time period (Friedlingstein et al., 2019) (Table 2). Additionally, we find reasonable agreement with the ocean interior carbon inversion estimate of −1.7 ± 0.4 Pg C year$^{-1}$ (nominal 1995) from Gruber et al. (2009); for year 1995, the ED estimate is −1.6 Pg C year$^{-1}$. ED, Röd13, and Land13 all demonstrate statistically significant trends in the global ocean $CO_2$ sink for 1995–2017, with trends of −0.065, −0.045, and −0.058 Pg C year$^{-2}$, respectively (supporting information Table S2). On the biome scale, Land13 has the largest number of biomes with statistically significant trends in air-sea $CO_2$ flux (14 out of 17 biomes), followed by ED (11 out of 17 biomes). Long-term air-sea $CO_2$ flux trends in Röd13 are less frequent (4 out of 17 biomes), likely due to the direct interpolation scheme of the mixed-layer method, which tends to extrapolate high-frequency noise in data-sparse regions and can result in larger interannual variability (Landschützer et al., 2015).

We find that the ED global ocean $CO_2$ sink (Figure 8, black line) generally lies within the envelope of the Röd13 and Land13 estimates (Figure 8, cyan and magenta lines; Table 2). Additionally, compared to many of the OBMs used to estimate the GCP ocean sink (Figure 8, orange thin lines), ED exhibits enhanced interannual and decadal-scale variability that is comparable to the interpolation-based products; these features are not typically captured in other OBM studies (Lovenduski et al., 2008; Sarmiento et al., 2010). These results suggest that ED, combined with the estimates from Röd13 and Land13, which have been previously shown to have the best fit to observations in their representation of global and tropical variability (Rödenbeck et al., 2015), could be used to form an improved uncertainty band for ocean carbon sink studies.
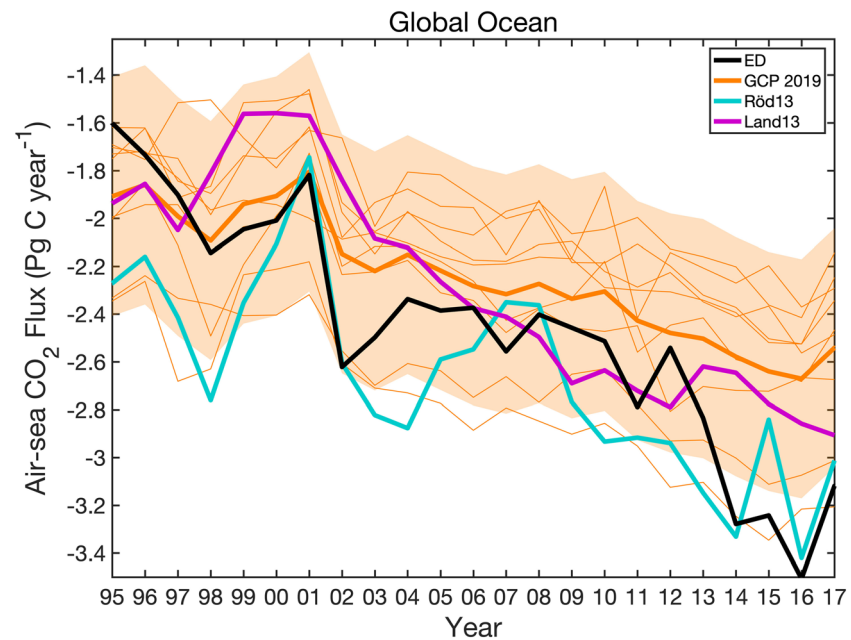
**Figure 8.** Globally integrated air-sea $CO_2$ flux time series for ED (black thick line), GCP 2019 ocean sink (orange thick line with uncertainty shown as shaded region), Röd13 (cyan thick line), and Land13 (magenta thick line). Air-sea $CO_2$ fluxes are annual means; all values represent uptake. Orange thin lines show the individual OBMs used to compute the GCP 2019 ocean sink.

*Note.* All values represent uptake; units are in petagram of carbon per year. Values represent temporal mean $\pm$ one standard deviation due to interannual variability. Error estimates for the GCP ocean sink include additional uncertainty (0.5 Pg C year$^{-1}$) from an ensemble of OBMs.

We observe the closest agreement between ED and the interpolation-based products in subtropical biomes (Figures 6 and 7, biomes 3, 4, 7, 10, 11, 13, and 14), albeit with ED often having a larger seasonal amplitude. This consistency between the model, complementary interpolation-based methods, and surface ocean $f$CO$_2$ observations (Figure A4) lends support to the estimates described here. Because subtropical surface ocean $p$CO$_2$ is strongly controlled by ocean temperature (Takahashi et al., 2002), we attribute this agreement to the ECCO LLC270 physics, which yield very realistic SST. In the equatorial Pacific Ocean, ED and the interpolation-based products show similar interannual variability, with a significant reduction in outgassing and surface ocean $p$CO$_2$ during ENSO events (Figure 7 and A2, biomes 5 and 6). These results suggest that ED is well suited for quantifying the drivers of air-sea $CO_2$ flux in the equatorial Pacific Ocean (Gierach et al., 2012, 2013), along with characterizing ENSO diversity (Capotondi et al., 2015). When integrated across the PEQU-W biome, ED outgassing is substantially reduced (e.g., 2010–2011) and/or completely arrested (e.g., 2015–2016) during onset/mature El Niño conditions (Figure 7, biome 5). In the PEQU-E biome, outgassing is prevalent during the entire period examined; here ED produces a weaker response to the 1997–1998 El Niño compared to Röd13 and Land13, along with showing a stronger decrease in outgassing for 2012–2017. While we find general agreement in equatorial Pacific Ocean air-sea $CO_2$ flux trends over interannual and longer timescales, there is substantial model-product mismatch in the seasonal cycle (Figures 6 and A2, biomes 5 and 6). We attribute this discrepancy to spatial gradients in ED surface ocean $p$CO$_2$ and air-sea $CO_2$ flux in these biomes (supporting information Figures S1 and S2), which are driven by model high-frequency ocean dynamics (i.e., tropical instability waves) and phytoplankton blooms that propagate westward from the Equatorial Islands (e.g., the Galapagos) (Gierach et al., 2013; Gove et al., 2016) and the coastal periphery of Central/South America.

The largest differences in long-term air-sea $CO_2$ fluxes between ED and the interpolation-based products occur in the Southern Ocean and North Pacific/Atlantic Oceans (Figures 2 and 7).

In the SO SPSS, the time-mean ED ocean $CO_2$ sink is a factor of ~2 and ~3 larger than Röd13 and Land13, respectively (Figure 7, biome 16). This results from strong winter uptake during March–August (Figure 6, biome 16), which biases the long-term $CO_2$ sink magnitude. In contrast, recent float-based observations from Gray et al. (2018) suggest significant winter outgassing between the polar front and marginal ice zone, which they attribute to the upwelling of nutrient- and carbon-rich waters. Our model results do not support this hypothesis, as Southern Ocean winter outgassing in ED is generally weak (supporting information Figure S7) and dominated by uptake when spatially integrated (Figures 6 and 7, biomes 15 and 16). We acknowledge that air-sea $CO_2$ fluxes in ED and the interpolation-based products are based on a simple parameterization of ocean-atmosphere exchange through leads; air-sea $CO_2$ flux is scaled by the open-water fraction of the ice cover. This parameterization may lead to the misrepresentation of biological productivity and air-sea gas exchange in regions affected by sea ice cover (e.g., Semiletov et al., 2004). Additionally, errors in the ECCO LLC270 representation of winter mixed layer dynamics in the Southern Ocean (see supporting information Figures S1–S5) could also be responsible for this mismatch.

While ED has a substantial air-sea $CO_2$ flux trend in SO STSS (~0.009 Pg C year$^{-1}$; supporting information Table S2), the simulation shows muted decadal-scale variability further south in SO SPSS (Figure 7, biome 16), similar to other OBM results (Lenton et al., 2013). In particular, ED does not show a weakening and subsequent reinvigoration of SO SPSS uptake for 2002–2011 (Gruber et al., 2019; Landschützer et al., 2015; Ritter et al., 2017); these trends are most pronounced in Land13 (Figure 7, biomes 16 and 17). We stress that while interpolation-based products suggest substantial decadal-scale variability in the Southern Ocean $CO_2$ sink, these estimates are accompanied by large uncertainties and time-space sampling biases. Further model development and evaluation, along with sustained year-round observations from Argo-BGC floats (Riser et al., 2018), are needed to further assess the fidelity of OBMs in the Southern Ocean.

In the NP SPSS biome, ED exhibits a smaller winter outgassing patch that lags the interpolation-based products by several months (supporting information Figures S1 and S2). The weaker outgassing patch, along with strong winter uptake (Figure 6, biome 2), biases ED toward larger long-term uptake compared to Röd13 and Land13 (Figure 7, biome 2). While the North Pacific Ocean is typically data rich for surface ocean $p$CO$_2$ (Bakker et al., 2016), substantial data gaps do occur in the observational record (Figures A4 and A5, biome 2), which could alias the surface ocean $p$CO$_2$ seasonal cycle and thus lead to weaker uptake in the interpolation-based products. Additionally, interactions between the Western Subarctic Gyre, Oyashio Current, and Bering and Okhotsk Sea outflows are typically not well resolved by OBMs (McKinley et al., 2006), which could also explain model-product differences in this region. We also observe similar patterns of mismatch between ED and the interpolation-based products in the North Atlantic Ocean, with ED having stronger winter ocean uptake in the NA SPSS (Figures 6 and 7, biome 9). The systematic bias of ED toward stronger winter uptake in subpolar seasonally stratified biomes, which results primarily from the competing influence of surface cooling and divergence in mixed layer DIC (Lauderdale et al., 2016), may result from the model's physical misrepresentation of seasonal mixed layer dynamics. We compared ED mixed layer depth with the observation-based product of Hosoda et al. (2010). For the 2004–2017 period, the simulated mixed layer at high latitudes is generally deeper during winter and shallower during summer than the Hosoda et al. (2010) product (supporting information Figures S1–S5). Future efforts focusing on understanding the underlying causes of model-product mismatch in these regions are critical for improving estimates of the global ocean $CO_2$ sink.

## 5. Summary and Concluding Remarks

We have developed ECCO-Darwin, a data-assimilative global ocean biogeochemistry model that allows for a quantitative multidecadal (1995–2017) description of the ocean's physical, chemical, and ecological state. Model physics are provided by the adjoint-based ECCO LLC270 circulation estimate, which assimilates nearly all available ocean observations since the era of satellite altimetry and has ~1/3° nominal horizontal grid spacing (~18 km at high latitudes). A low-dimensional Green's functions approach (adjusting biogeochemical initial conditions and six model parameters) is used to improve model fit to global biogeochemical observations in a property-conserving manner (i.e., without nudging or generating spurious sources/sinks). We then use ECCO-Darwin, along with a suite of interpolation-based products, to estimate seasonal to multidecadal surface ocean $p$CO$_2$ and air-sea $CO_2$ fluxes across the global ocean and in 17 open-ocean biomes.

Modeled air-sea $CO_2$ fluxes show broad-scale consistency with surface ocean $pCO_2$ observations and interpolation-based products in many biomes. The closest agreement occurs in the subtropical and equatorial regions. The largest disagreement occurs in subpolar regions that are characterized by large seasonal variations in mixed layer depth and where ECCO-Darwin has, in general, stronger winter uptake than the interpolation-based products. Compared to other ocean biogeochemical models, ECCO-Darwin has a global ocean $CO_2$ sink that agrees well with interpolation-based products in terms of both magnitude (time mean of $-2.47 \pm 0.50$ Pg C year$^{-1}$) and temporal variability.

While ED already provides a promising model-based framework for investigating air-sea CO2 fluxes and ocean carbon cycling, there are several areas where model and data assimilation can be substantially improved. (1) *Land-ocean aquatic continuum:* Terrestrial runoff for rivers, ice sheets, and groundwater are coarsely represented in ED, do not contain nutrients and organic carbon, and do not interact with coastal ecosystems. Ongoing ED model development aims to add time-varying global biogeochemical runoff and to better parameterize coastal ecosystems in order to improve the representation of coastal (Chen et al., 2013; Cotrim da Cunha et al., 2007) and ice sheet processes (Hopwood et al., 2018). (2) *Dissolution rate and bottom sediments:* Our treatment of calcium carbonate does not currently include nonlinear dissolution rate laws (Naviaux et al., 2019; Subhas et al., 2015) or account for sediment burial (Dunne et al., 2012). Improved parameterizations for these processes are required in order to better represent ocean acidification. (3) *Mesoscale and submesoscale processes:* The current nominal 1/3° horizontal grid spacing of ED does not permit explicit representation of mesoscale eddies, let alone submesoscale ocean processes. As it becomes computationally practical, we expect that increased ED model resolution will permit an increasingly more realistic representation of mesoscale and submesoscale physical-biogeochemical interactions. (4) *Satellite and airborne observations of ocean color:* Although we have not yet included ocean color data constraints in ED, the Darwin ocean ecology package already includes a radiative transfer module (Dutkiewicz et al., 2015), which will permit the direct utilization of satellite and airborne ocean color observations for evaluation and adjustment of ED. Future data assimilation development will include these important data constraints, with potential to improve phytoplankton phenology and thus improve the timing and magnitude of blooms. (5) *Adjoint method optimization:* In this study, we rely on a low-dimensional Green's functions approach to minimize biogeochemical model-data misfit; the incorporation of an adjoint-based optimization method, as is done by Verdy and Mazloff (2017) for the Southern Ocean, would allow for a larger number of control variables and for joint physical-biogeochemical optimization. Adjoint-method optimization will permit a much larger number of control variables than is possible with the Green's functions approach and hence a closer fit of ED to biogeochemical observations. Furthermore, adjoint-method optimization of the coupled physical-biogeochemical model will allow the use of biogeochemical observations for adjusting ocean physics. (6) *Formal uncertainty estimates:* In this manuscript we have presented a preliminary comparison with observations and observation-based products. These results suggest that ECCO-Darwin, combined with complementary interpolation-based products, can be used to form improved uncertainty estimates for ocean carbon sink studies. In particular, synthetic observations, formed by sampling ECCO-Darwin at the locations and times of available observations and adding geophysical noise, can be used to evaluate sampling biases in the interpolation-based approaches. We acknowledge that the ED simulation presented in this paper is at best eddy permitting, so this evaluation may overestimate the representation of observations required. Conversely, the interpolation-based approaches will allow us to identify and reduce ED model deficiencies.

Despite the above limitations, many of which are already being actively addressed, our modeling efforts provide a significant step forward in the development of a global ocean physical and biogeochemical estimation framework. The solution presented herein has been made available on a data server and is already beginning to be used for science and practical applications, for example, by the Carbon Monitoring System Flux project. Of equally high significance is that the model and analysis software have also been carefully documented and made available in public code repositories and therefore can be used or further developed by other researchers. As the ECCO ocean state estimates, the Darwin Project ocean ecology and biogeochemistry, and interactions between these two projects and other climate components continue to evolve, we expect ECCO-Darwin to become an ever more accurate and useful tool in support of ocean carbon, marine ecosystem, and climate-related studies.

## Appendix A: Model-Data Comparisons in Open Ocean Biomes

Figure A1 illustrates the geographical extent of the 17 open-ocean biomes used in this study. Figures A2–A5 provide some additional model-data comparisons in these 17 biomes.
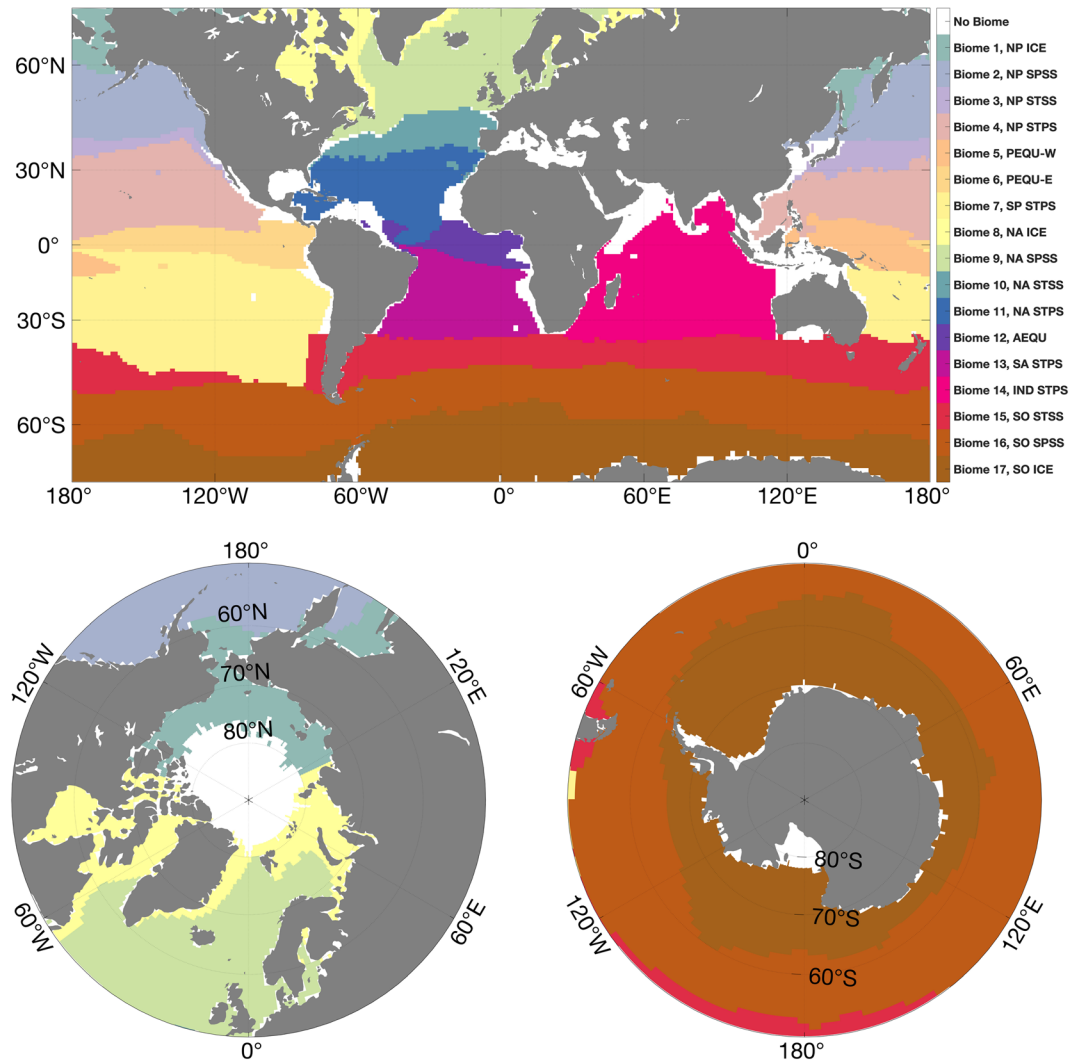


**Figure A1.** Fay and McKinley (2014) open-ocean biomes used to compute area-weighted mean surface ocean $p$CO$_2$ and spatially integrated air-sea CO$_2$ fluxes; biomes are interpolated to the ED model grid. Acronyms refer to polar regions (ICE), sub-polar seasonally stratified (SPSS), sub-tropical seasonally stratified (STSS), and sub-tropical permanently stratified (STPS) biomes in the North Pacific (NP), South Pacific (SP), North Atlantic (NA), South Atlantic (SA), Indian Ocean (IND), Southern Ocean (SO), as well as the Atlantic equatorial (AEQU) and the West and East Pacific equatorial (PEQU-W and PEQU-E, respectively) biomes.
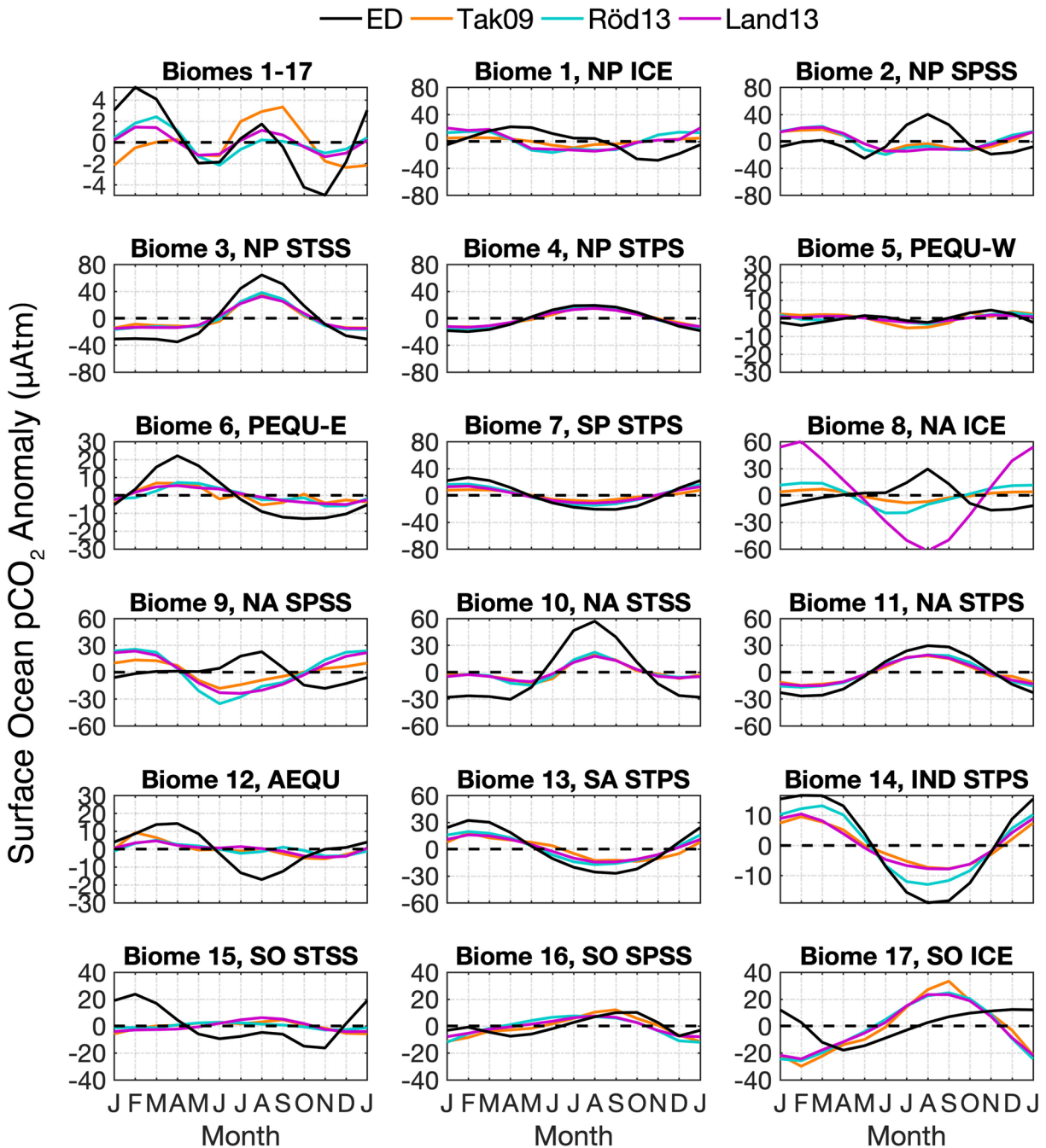
**Figure A2.** Seasonal cycle of surface ocean $p\text{CO}_2$ for each biome. Surface ocean $p\text{CO}_2$ is time averaged for each month (for January 1995 to December 2017) and represents the area-weighted mean for each biome. Anomalies with respect to the long-term mean are shown. Similar $y$ axis scales are used for each individual ocean basin.
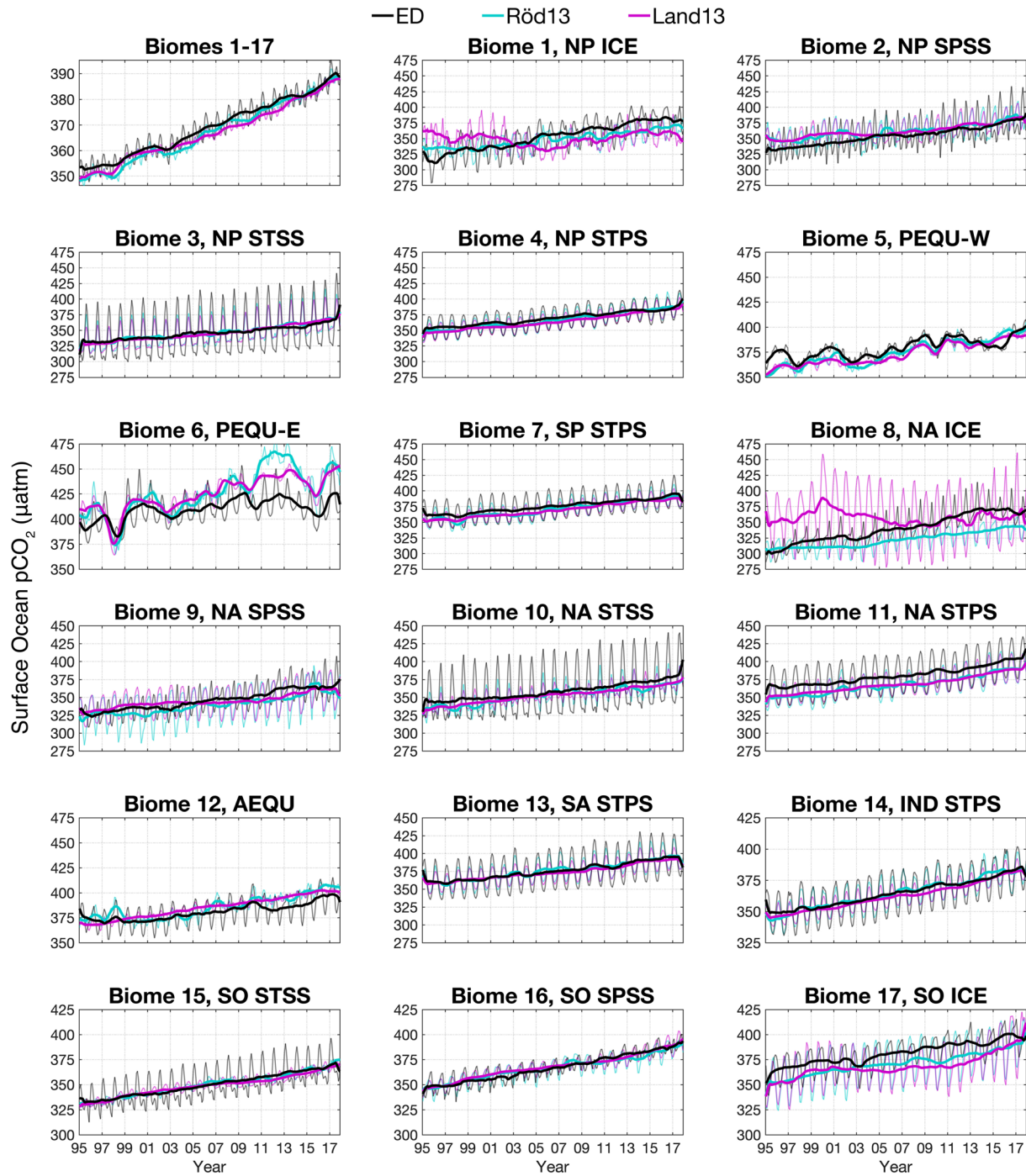
**Figure A3.** Monthly surface ocean $p$CO$_2$ time series for ED (black), Röd13 (cyan), and Land13 (magenta). Surface ocean $p$CO$_2$ represents the area-weighted mean for each biome. Thin lines show monthly values and thick lines show interannual variability (12-month running mean). Similar $y$ axis scales are used for each individual ocean basin.
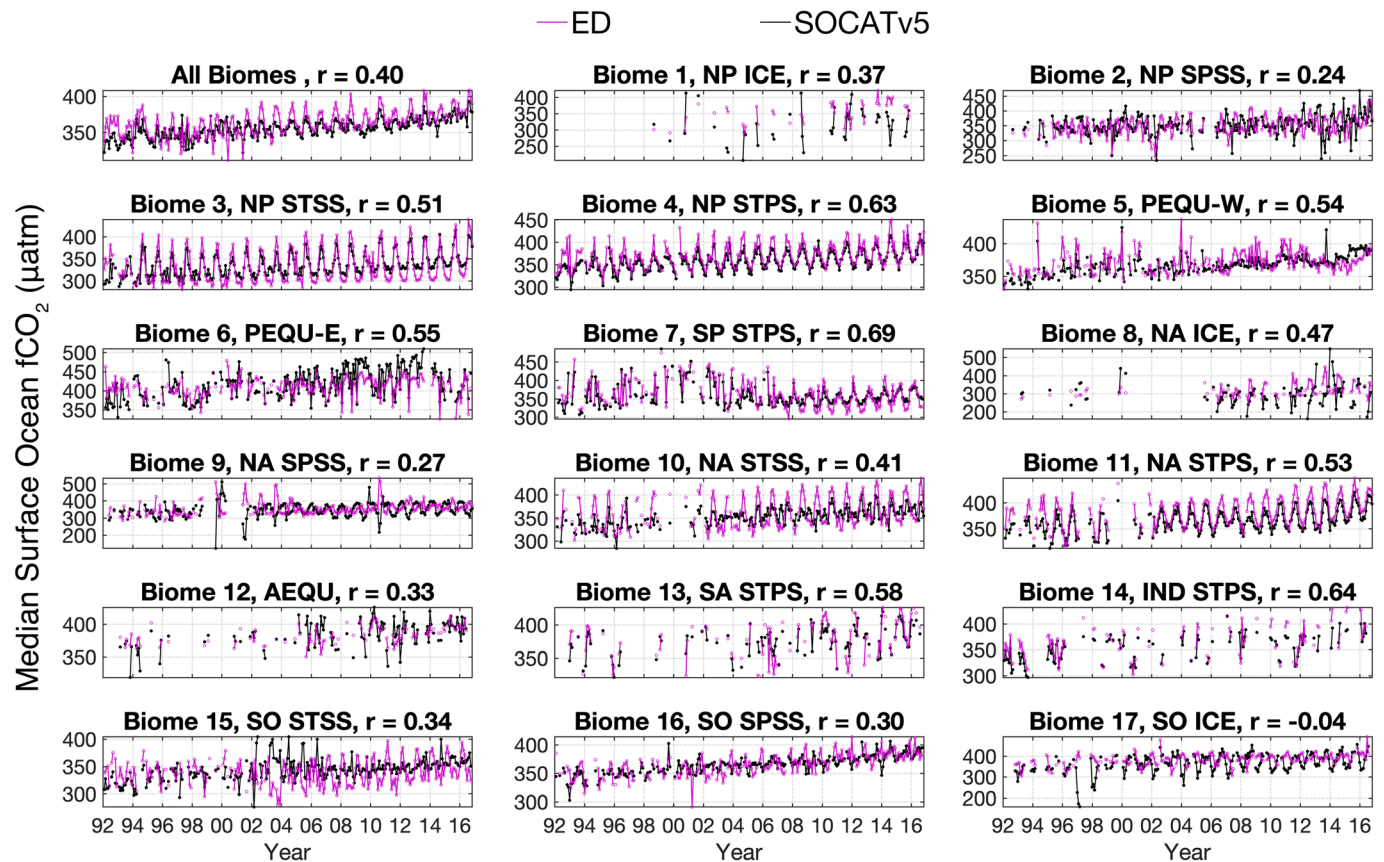
**Figure A4.** Monthly time series of surface ocean $f$CO$_2$ for SOCATv5 (black) and corresponding ED values (magenta) taken at the same time-space locations over the optimization period. Median monthly values for each biome are shown. Adjacent monthly values without data gaps are connected with solid lines. ED-SOCATv5 correlation coefficients (for all prewhitened monthly values) over the entire time period are shown above each panel.
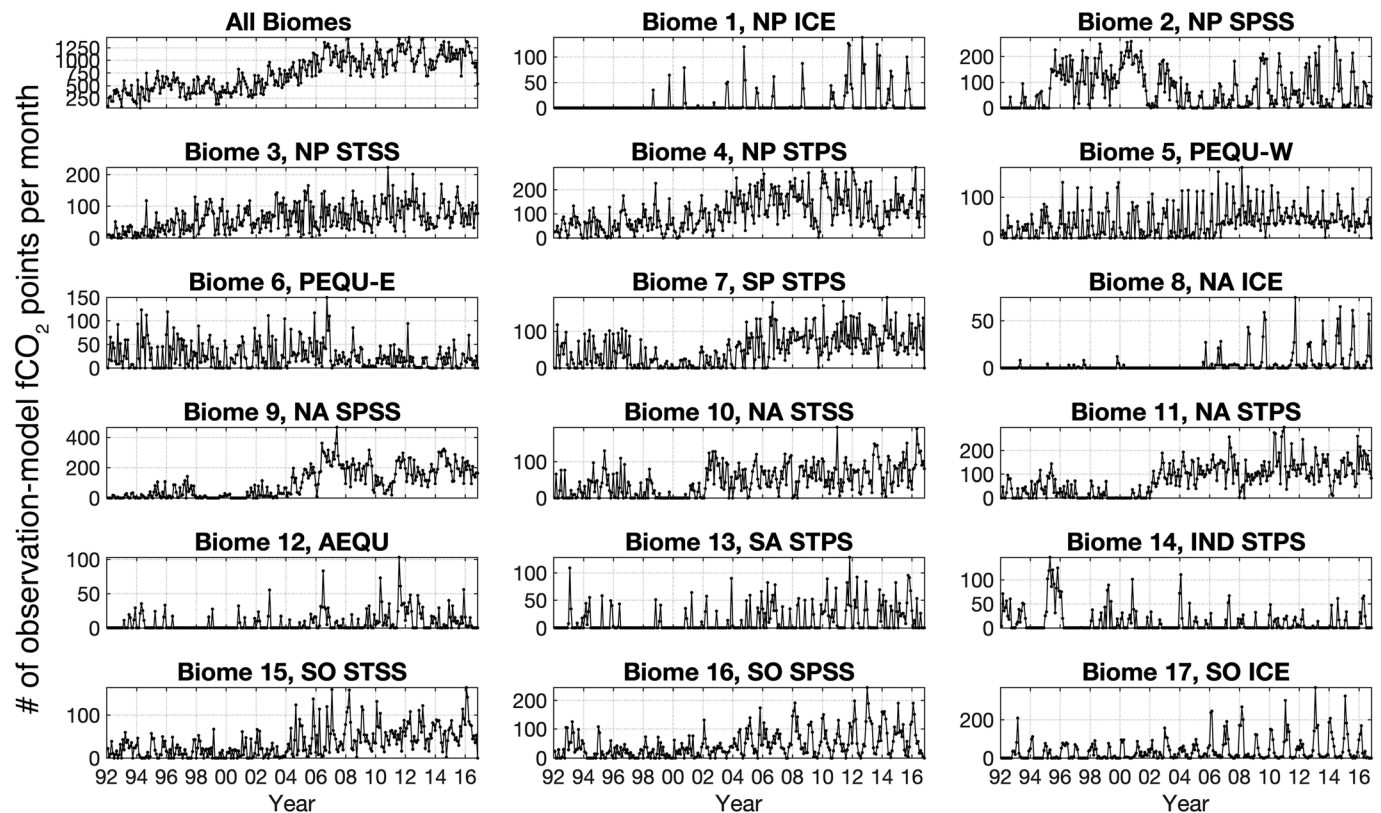
**Figure A5.** Number of observed surface ocean $f$CO$_2$ points per month for each biome over the optimization period.

## Data Availability Statement

ECCO-Darwin model fields are available at the website (https://data.nas.nasa.gov/ecco). Platform-independent instructions for running ECCO-Darwin simulations are available at the website (https://zenodo.org/badge/doi/10.5281/zenodo.3829965.svg). Copyright 2020 California Institute of Technology. U.S. Government sponsorship acknowledged. All rights reserved.

## References

Andersen, O., Knudsen, P., & Stenseng, L. (2016). The DTU13 MSS (mean sea surface) and MDT (mean dynamic topography) from 20 years of satellite altimetry. In *IGFS 2014* (pp. 111–121). Cham: Springer International Publishing.

Andrews, A. E., Kofler, J. D., Trudeau, M. E., Williams, J. C., Neff, D. H., Masarie, K. A., et al. (2014). CO$_2$, CO, and CH$_4$ measurements from tall towers in the NOAA Earth System Research Laboratory's global greenhouse gas reference network: Instrumentation, uncertainty analysis, and recommendations for future high-accuracy greenhouse gas monitoring efforts. *Atmospheric Measurement Techniques*, 7(2), 647–687. https://doi.org/10.5194/amt-7-647-2014

Antonov, J., Seidov, D., Boyer, T., Locarnini, R., Mishonov, A., & Garcia, H. (2010). *World Ocean Atlas 2009 Volume 2: Salinity, NOAA Atlas NESDIS 69*. Washington, DC: U.S. Government Printing Office.

Aumont, O., Ethé, C., Tagliabue, A., Bopp, L., & Gehlen, M. (2015). PISCES-v2: An ocean biogeochemical model for carbon and ecosystem studies. *Geoscientific Model Development*, 8(8), 2465–2513. https://doi.org/10.5194/gmd-8-2465-2015

Bakker, D. C. E., Pfeil, B., Landa, C. S., Metzl, N., O'Brien, K. M., Olsen, A., et al. (2016). A multidecade record of high-quality $f$CO$_2$ data in version 3 of the Surface Ocean CO$_2$ Atlas (SOCAT). *Earth System Science Data*, 8(2), 383–413. https://doi.org/10.5194/essd-8-383-2016

Bakker, D. C. E., Pfeil, B., Smith, K., Hankin, S., Olsen, A., Alin, S. R., et al. (2014). An update to the Surface Ocean CO$_2$ Atlas (SOCAT version 2). *Earth System Science Data*, 6(1), 69–90. https://doi.org/10.5194/essd-6-69-2014

Bates, N. R., Astor, Y. M., Church, M. J., Currie, K., Dore, J. E., González-Dávila, M., et al. (2014). A time-series view of changing ocean chemistry due to ocean uptake of anthropogenic CO$_2$ and ocean acidification. *Oceanography*, 27(1), 126–141. https://doi.org/10.5670/oceanog.2014.16

Bowman, K. W., Liu, J., Bloom, A. A., Parazoo, N. C., Lee, M., Jiang, Z., et al. (2017). Global and Brazilian carbon response to El Niño Modoki 2011–2010. *Earth and Space Science*, 4, 637–660. https://doi.org/10.1002/2016EA000204

Brix, H., Menemenlis, D., Hill, C., Dutkiewicz, S., Jahn, O., Wang, D., & Zhang, H. (2015). Using Green's functions to initialize and adjust a global, eddying ocean biogeochemistry general circulation model. *Ocean Modelling*, 95, 1–14. https://doi.org/10.1016/j.ocemod.2015.07.008

Capotondi, A., Wittenberg, A. T., Newman, M., di Lorenzo, E., Yu, J. Y., Braconnot, P., et al. (2015). Understanding ENSO diversity. *Bulletin of the American Meteorological Society*, *96*(6), 921–938. https://doi.org/10.1175/BAMS-D-13-00117.1

Chen, C. T. A., Huang, T. H., Chen, Y. C., Bai, Y., He, X., & Kang, Y. (2013). Air-sea exchanges of $CO_2$ in the world's coastal seas. *Biogeosciences*, *10*(10), 6509–6544. https://doi.org/10.5194/bg-10-6509-2013

Ciais, P., Sabine, C., Bala, G., Bopp, L., Brovkin, V., Canadell, J., et al. (2013). Carbon and other biogeochemical cycles supplementary material. In T. F. Stocker et al. (Eds.), *Climate Change 2013: The Physical Science Basis. Contribution of Working Group I to the Fifth Assessment Report of the Intergovernmental Panel on Climate Change* (pp. 465–570). Cambridge, UK and New York, NY: Cambridge University Press.

Cotrim da Cunha, L., Buitenhuis, E. T., Le Quéré, C., Giraud, X., & Ludwig, W. (2007). Potential impact of changes in river nutrient supply on global ocean biogeochemistry. *Global Biogeochemical Cycles*, *21*, GB4007. https://doi.org/10.1029/2006gb002718

Dee, D. P., Uppala, S. M., Simmons, A. J., Berrisford, P., Poli, P., Kobayashi, S., et al. (2011). The ERA-interim reanalysis: Configuration and performance of the data assimilation system. *Quarterly Journal of the Royal Meteorological Society*, *137*(656), 553–597. https://doi.org/10.1002/qj.828

DeVries, T. (2014). The oceanic anthropogenic $CO_2$ sink: Storage, air-sea fluxes, and transports over the industrial era. *Global Biogeochemical Cycles*, *28*, 631–647. https://doi.org/10.1002/2013GB004739

DeVries, T., Holzer, M., & Primeau, F. (2017). Recent increase in oceanic carbon uptake driven by weaker upper-ocean overturning. *Nature*, *542*(7640), 215–218. https://doi.org/10.1038/nature21068

DeVries, T., Le Quéré, C., Andrews, O., Berthet, S., Hauck, J., Ilyina, T., et al. (2019). Decadal trends in the ocean carbon sink. *Proceedings. National Academy of Sciences. United States of America*, *116*(24), 11,646–11,651. https://doi.org/10.1073/pnas.1900371116

Dore, J. E., Lukas, R., Sadler, D. W., Church, M. J., & Karl, D. M. (2009). Physical and biogeochemical modulation of ocean acidification in the central North Pacific. *Proceedings. National Academy of Sciences. United States of America*, *106*(30), 12,235–12,240. https://doi.org/10.1073/pnas.0906044106

Drucker, R., & Riser, S. C. (2016). In situ phase-domain calibration of oxygen optodes on profiling floats. *Methods in Oceanography*, *17*, 296–318. https://doi.org/10.1016/j.mio.2016.09.007

Dunne, J. P., Hales, B., & Toggweiler, J. R. (2012). Global calcite cycling constrained by sediment preservation controls. *Global Biogeochemical Cycles*, *26*, GB3023. https://doi.org/10.1029/2010GB003935

Dutkiewicz, S., Follows, M. J., & Bragg, J. G. (2009). Modeling the coupling of ocean ecology and biogeochemistry. *Global Biogeochemical Cycles*, *23*, GB4017. https://doi.org/10.1029/2008GB003405

Dutkiewicz, S., Hickman, A. E., Jahn, O., Gregg, W. W., Mouw, C. B., & Follows, M. J. (2015). Capturing optically important constituents and properties in a marine biogeochemical and ecosystem model. *Biogeosciences*, *12*(14), 4447–4481. https://doi.org/10.5194/bg-12-4447-2015

Dutkiewicz, S., Ward, B. A., Scott, J., & Follows, M. J. (2014). Understanding predicted shifts in diazotroph biogeography using resource competition theory. *Biogeosciences*, *11*(19), 5445–5461. https://doi.org/10.5194/bg-11-5445-2014

Fay, A. R., & McKinley, G. A. (2013). Global trends in surface ocean $p$$CO_2$ from in situ data. *Global Biogeochemical Cycles*, *27*, 541–557. https://doi.org/10.1002/gbc.20051

Fay, A. R., & McKinley, G. A. (2014). Global open-ocean biomes: Mean and temporal variability. *Earth System Science Data*, *6*(2), 273–284. https://doi.org/10.5194/essd-6-273-2014

Fay, A. R., McKinley, G. A., & Lovenduski, N. S. (2014). Southern Ocean carbon trends: Sensitivity to methods. *Geophysical Research Letters*, *41*, 6833–6840. https://doi.org/10.1002/2014GL061324

Feely, R. A., Takahashi, T., Wanninkhof, R., McPhaden, M. J., Cosca, C. E., Sutherland, S. C., & Carr, M. E. (2006). Decadal variability of the air-sea $CO_2$ fluxes in the equatorial Pacific Ocean. *Journal of Geophysical Research*, *111*, C08S90. https://doi.org/10.1029/2005JC003129

Fekete, B. M., Vöröosmarty, C. J., & Grabs, W. (2002). High-resolution fields of global runoff combining observed river discharge and simulated water balances. *Global Biogeochemical Cycles*, *16*(3), 1042. https://doi.org/10.1029/1999GB001254

Fenty, I., Menemenlis, D., & Zhang, H. (2017). Global coupled sea ice-ocean state estimation. *Climate Dynamics*, *49*(3), 931–956. https://doi.org/10.1007/s00382-015-2796-6

Follows, M. J., & Dutkiewicz, S. (2011). Modeling diverse communities of marine microbes. *Annual Review of Marine Science*, *3*(1), 427–451. https://doi.org/10.1146/annurev-marine-120709-142848

Follows, M. J., Dutkiewicz, S., Grant, S., & Chisholm, S. W. (2007). Emergent biogeography of microbial communities in a model ocean. *Science*, *315*(5820), 1843–1846. https://doi.org/10.1126/science.1138544

Follows, M. J., Dutkiewicz, S., & Ito, T. (2006). On the solution of the carbonate system in ocean biogeochemistry models. *Ocean Modelling*, *12*(3-4), 290–301. https://doi.org/10.1016/j.ocemod.2005.05.004

Forget, G., Campin, J., Heimbach, P., Hill, C. N., Ponte, R., & Wunsch, C. (2015). ECCO version 4: An integrated framework for non-linear inverse modeling and global ocean state estimation. *Geoscientific Model Development*, *8*(10), 3071–3104. https://doi.org/10.5194/gmd-8-3071-2015

Forget, G., & Ponte, R. M. (2015). The partition of regional sea level variability. *Progress in Oceanography*, *137*, 173–195. https://doi.org/10.1016/j.pocean.2015.06.002

Friedlingstein, P., Jones, M. W., O'Sullivan, M., Andrew, R. M., Hauck, J., Peters, G. P., et al. (2019). Global carbon budget 2019. *Earth System Science Data*, *11*(4), 1783–1838. https://doi.org/10.5194/essd-11-1783-2019

Galbraith, E. D., Gnanadesikan, A., Dunne, J. P., & Hiscock, M. R. (2010). Regional impacts of iron-light colimitation in a global biogeochemical model. *Biogeosciences*, *7*(3), 1043–1064. https://doi.org/10.5194/bg-7-1043-2010

Gent, P., & McWilliams, J. (1990). Isopycnal mixing in ocean circulation models. *Journal of Physical Oceanography*, *20*(1), 150–155. https://doi.org/10.1175/1520-0485(1990)020<0150:IMIOCM>2.0.CO;2

Gierach, M. M., Lee, T., Turk, D., & McPhaden, M. J. (2012). Biological response to the 1997–98 and 2009–10 El Niño events in the equatorial Pacific Ocean. *Geophysical Research Letters*, *39*, L10602. https://doi.org/10.1029/2012GL051103

Gierach, M. M., Messié, M., Lee, T., Karnauskas, K. B., & Radenac, M.-H. (2013). Biophysical responses near Equatorial Islands in the Western equatorial Pacific Ocean during El Niño/La Niña transitions. *Geophysical Research Letters*, *40*, 5473–5479. https://doi.org/10.1002/2013GL057828

Gilbert, R. (1987). *Statistical Methods for Environmental Pollution Monitoring* (p. 320). New York: Van Nostrand Reinhold.

Gove, J. M., McManus, M. A., Neuheimer, A. B., Polovina, J. J., Drazen, J. C., Smith, C. R., et al. (2016). Near-island biological hotspots in barren ocean basins. *Nature Communications*, *7*(1), 10,581. https://doi.org/10.1038/ncomms10581

Gray, A. R., Johnson, K. S., Bushinsky, S. M., Riser, S. C., Russell, J. L., Talley, L. D., et al. (2018). Autonomous biogeochemical floats detect significant carbon dioxide outgassing in the high-latitude Southern Ocean. *Geophysical Research Letters*, *45*(17), 9049–9057. https://doi.org/10.1029/2018GL078013

Gruber, N., Gloor, M., Mikaloff Fletcher, S. E., Doney, S. C., Dutkiewicz, S., Follows, M. J., et al. (2009). Oceanic sources, sinks, and transport of atmospheric $CO_2$. *Global Biogeochemical Cycles*, *23*, GB1005. https://doi.org/10.1029/2008gb003349

Gruber, N., Keeling, C. D., & Bates, N. R. (2002). Interannual variability in the North Atlantic Ocean carbon sink. *Science*, *298*(5602), 2374–2378. https://doi.org/10.1126/science.1077077

Gruber, N., Landschützer, P., & Lovenduski, N. S. (2019). The variable Southern Ocean carbon sink. *Annual Review of Marine Science*, *11*(1), 159–186. https://doi.org/10.1146/annurev-marine-121916-063407

Hamed, K. H., & Rao, A. R. (1998). A modified Mann-Kendall trend test for autocorrelated data. *Journal of Hydrology*, *204*(1-4), 182–196. https://doi.org/10.1016/S0022-1694(97)00125-X

Hopwood, M. J., Carroll, D., Browning, T. J., Meire, L., Mortensen, J., Krisch, S., & Achterberg, E. P. (2018). Non-linear response of summertime marine productivity to increased meltwater discharge around Greenland. *Nature Communications*, *9*(1), 3256. https://doi.org/10.1038/s41467-018-05488-8

Hosoda, S., Ohira, T., Sato, K., & Suga, T. (2010). Improved description of global mixed-layer depth using Argo profiling floats. *Journal of Oceanography*, *66*(6), 773–787. https://doi.org/10.1007/s10872-010-0063-3

IPCC (2013). In T. F. Stocker, et al. (Eds.), *Climate Change 2013: The Physical Science Basis. Contribution of Working Group I to the Fifth Assessment Report of the Intergovernmental Panel on Climate Change* (p. 1535). Cambridge, United Kingdom and New York, NY, USA: Cambridge University press.

Ito, T., & Follows, M. J. (2013). Air-sea disequilibrium of carbon dioxide enhances the biological carbon sequestration in the Southern Ocean. *Global Biogeochemical Cycles*, *27*, 1129–1138. https://doi.org/10.1002/2013GB004682

Kendall, M. G. (1975). *Rank Correlation Methods*. London: Griffin.

Khatiwala, S., Primeau, F., & Hall, T. (2009). Reconstruction of the history of anthropogenic $CO_2$ concentrations in the ocean. *Nature*, *462*(7271), 346–349. https://doi.org/10.1038/nature08526

Khatiwala, S., Tanhua, T., Mikaloff Fletcher, S., Gerber, M., Doney, S. C., Graven, H. D., et al. (2013). Global ocean storage of anthropogenic carbon. *Biogeosciences*, *10*(4), 2169–2191. https://doi.org/10.5194/bg-10-2169-2013

Khazendar, A., Fenty, I., Carroll, D., Gardner, A., Fukumori, I., Wang, O., et al. (2019). Interruption of two decades of Jakobshavn Isbrae acceleration and thinning as regional ocean cools. *Nature Geoscience*, *12*(4), 277–283. https://doi.org/10.1038/s41561-019-0329-3

Krishfield, R., Toole, J., Proshutinsky, A., & Timmermans, M.-L. (2008). Automated ice-tethered profilers for seawater observations under pack ice in all seasons. *Journal of Atmospheric and Oceanic Technology*, *25*(11), 2091–2105. https://doi.org/10.1175/2008JTECHO587.1

Kunze, E. (2019). Biologically generated mixing in the ocean. *Annual Review of Marine Science*, *11*(1), 215–226. https://doi.org/10.1146/annurev-marine-010318-095047

Landschützer, P., Gruber, N., Bakker, D., & Schuster, U. (2014). Recent variability of the global ocean carbon sink. *Global Biogeochemical Cycles*, *28*, 927–949. https://doi.org/10.1002/2014GB004853

Landschützer, P., Gruber, N., & Bakker, D. C. E. (2016). Decadal variations and trends of the global ocean carbon sink. *Global Biogeochemical Cycles*, *30*, 1396–1417. https://doi.org/10.1002/2015GB005359

Landschützer, P., Gruber, N., Bakker, D., Schuster, U., Nakaoka, S., Payne, M. R., et al. (2013). A neural network-based estimate of the seasonal to inter-annual variability of the Atlantic Ocean carbon sink. *Biogeosciences*, *10*(11), 7793–7815. https://doi.org/10.5194/bg-10-7793-2013

Landschützer, P., Gruber, N., Bakker, D. C. E., Stemmler, I., & Six, K. D. (2018). Strengthening seasonal marine $CO_2$ variations due to increasing atmospheric $CO_2$. *Nature Climate Change*, *8*(2), 146–150. https://doi.org/10.1038/s41558-017-0057-x

Landschützer, P., Gruber, N., Haumann, F. A., Rödenbeck, C., Bakker, D. C. E., van Heuven, S., et al. (2015). The reinvigoration of the Southern Ocean carbon sink. *Science*, *349*(6253), 1221–1224. https://doi.org/10.1126/science.aab2620

Lauderdale, J. M., Dutkiewicz, S., Williams, R. G., & Follows, M. J. (2016). Quantifying the drivers of ocean-atmosphere $CO_2$ fluxes. *Global Biogeochemical Cycles*, *30*, 983–999. https://doi.org/10.1002/2016GB005400

Lenton, A., Tilbrook, B., Law, R. M., Bakker, D., Doney, S. C., Gruber, N., et al. (2013). Sea–air CO2 fluxes in the Southern Ocean for the period 1990–2009. *Biogeosciences*, *10*, 4037–4054. https://doi.org/10.5194/bg-10-4037-2013

Le Quéré, C., Aumont, O., Bopp, L., Bousquet, P., Ciais, P., Francey, R., et al. (2003). Two decades of ocean $CO_2$ sink and variability. *Tellus Series B*, *55*(2), 649–656. https://doi.org/10.3402/tellusb.v55i2.16719

Le Quéré, C., Takahashi, T., Buitenhuis, E. T., Rödenbeck, C., & Sutherland, S. C. (2010). Impact of climate change and variability on the global oceanic sink of $CO_2$. *Global Biogeochemical Cycles*, *24*, GB4007. https://doi.org/10.1029/2009gb003599

Le Quéré, C., Andrew, R. M., Friedlingstein, P., Sitch, S., Hauck, J., Pongratz, J., et al. (2018). Global carbon budget 2018. *Earth System Science Data*, *10*(4), 2141–2194. https://doi.org/10.5194/essd-10-2141-2018

Liu, J., Bowman, K., Lee, M., Henze, D., Bousserez, N., Brix, H., et al. (2014). Carbon monitoring system flux estimation and attribution: Impact of ACOS-GOSAT $X_{CO2}$ sampling on the inference of terrestrial biospheric sources and sinks. *Tellus Series B*, *66*(1), 22,486. https://doi.org/10.3402/tellusb.v66.22486

Liu, J., Bowman, K. W., Schimel, D. S., Parazoo, N. C., Jiang, Z., Lee, M., et al. (2017). Contrasting carbon cycle responses of the tropical continents to the 2015–2016 El Nino. *Science*, *358*(6360), eaam5690. https://doi.org/10.1126/science.aam5690

Locarnini, R. A., Mishonov, A. V., Antonov, J. I., Boyer, T. P., Garcia, H. E., Baranova, O. K., et al. (2010). World Ocean Atlas 2009, volume 1: Temperature. In S. Levitus (Ed.), *NOAA Atlas NESDIS 68* (184 pp.). Washington, DC: U.S. Government Printing Office.

Lovenduski, N., Gruber, N., & Doney, S. C. (2008). Towards a mechanistic understanding of the decadal trends in the Southern Ocean carbon sink. *Global Biogeochemical Cycles*, *22*, GB3016. https://doi.org/10.1029/2007GB003139

Lovenduski, N. S., Fay, A. R., & McKinley, G. A. (2015). Observing multi-decadal trends in Southern Ocean $CO_2$ uptake: What can we learn from an ocean model? *Global Biogeochemical Cycles*, *29*, 416–426. https://doi.org/10.1002/2014GB004933

Lovenduski, N. S., McKinley, G. A., Fay, A. R., Lindsay, K., & Long, M. C. (2016). Partitioning uncertainty in ocean carbon uptake projections: Internal variability, emission scenario, and model structure. *Global Biogeochemical Cycles*, *30*, 1276–1287. https://doi.org/10.1002/2016GB005426

Mahowald, N. M., Engelstaedter, S., Luo, C., Sealy, A., Artaxo, P., Benitez-Nelson, C., et al. (2009). Atmospheric iron deposition: Global distribution, variability, and human perturbations. *Annual Review of Marine Science*, *1*(1), 245–278. https://doi.org/10.1146/annurev.marine.010908.163727

Mann, H. B. (1945). Non-parametric tests against trend. *Econometrica*, *13*(3), 245–259. https://doi.org/10.2307/1907187

Marshall, J., Adcroft, A., Hill, C., Perelman, L., & Heisey, C. (1997). A finite-volume, incompressible Navier-Stokes model for studies of the ocean on parallel computers. *Journal of Geophysical Research*, *102*(C3), 5753–5766. https://doi.org/10.1029/96JC02775

Martin, J., & Fitzwater, S. (1988). Iron deficiency limits phytoplankton growth in the north-East Pacific subarctic. *Nature*, *331*(6154), 341–343. https://doi.org/10.1038/331341a0

McKinley, G. A., Fay, A. R., Lovenduski, N. S., & Pilcher, D. J. (2017). Natural variability and anthropogenic trends in the ocean carbon sink. *Annual Review of Marine Science*, *9*(1), 125–150. https://doi.org/10.1146/annurev-marine-010816-060529

McKinley, G. A., Pilcher, D. J., Fay, A. R., Lindsay, K., Long, M. C., & Lovenduski, N. (2016). Timescales for detection of trends in the ocean carbon sink. *Nature*, *530*(7591), 469–472. https://doi.org/10.1038/nature16958

McKinley, G. A., Takahashi, T., Buitenhuis, E., Chai, F., Christian, J. R., Doney, S. C., et al. (2006). North Pacific carbon cycle response to climate variability on seasonal to decadal timescales. *Journal of Geophysical Research*, *111*, C07S06. https://doi.org/10.1029/2005JC003173

Meier, W., Fetterer, F., Savoie, M, Mallory, S., Duerr, R., & Stroeve, J. (2017). NOAA/NSIDC Climate Data Record of passive microwave sea ice concentration, version 3, https://nsidc.org/data/G02202

Menemenlis, D., Campin, J., Heimbach, P., Hill, C., Lee, T., Nguyen, A., et al. (2008). ECCO2: High resolution global ocean and sea ice data synthesis. *Mercator Ocean Quart. Newsletter*, *31*, 13–21.

Menemenlis, D., Fukumori, I., & Lee, T. (2005). Using Green's functions to calibrate an ocean general circulation model. *Monthly Weather Review*, *133*(5), 1224–1240. https://doi.org/10.1175/MWR2912.1

Mikaloff Fletcher, S. E., Gruber, N., Jacobson, A. R., Doney, S. C., Dutkiewicz, S., Gerber, M., et al. (2006). Inverse estimates of anthropogenic $CO_2$ uptake, transport, and storage by the ocean. *Global Biogeochemical Cycles*, *20*, GB2002. https://doi.org/10.1029/2005GB002530

Munro, D. R., Lovenduski, N. S., Takahashi, T., Stephens, B. B., Newberger, T., & Sweeney, C. (2015). Recent evidence for a strengthening $CO_2$ sink in the Southern Ocean from carbonate system measurements in the Drake Passage (2002–2015). *Geophysical Research Letters*, *42*, 7623–7630. https://doi.org/10.1002/2015GL065194

Nakayama, Y., Manucharyan, G., Zhang, H., Dutrieux, P., Torres, H. S., Klein, P., et al. (2019). Pathways of ocean heat towards Pine Island and Thwaites grounding lines. *Scientific Reports*, *9*(1), 16,649. https://doi.org/10.1038/s41598-019-53190-6

Nakayama, Y., Menemenlis, D., Schodlok, M. P., & Rignot, E. J. (2017). Amundsen and Bellingshausen seas simulation with Optimized Ocean, sea ice, and thermodynamic ice shelf model parameters. *Journal of Geophysical Research: Oceans*, *122*, 6180–6195. https://doi.org/10.1002/2016JC012538

Nakayama, Y., Menemenlis, D., Zhang, H., Schodlok, M., & Rignot, E. (2018). Origin of circumpolar deep water intruding onto the Amundsen and Bellingshausen Sea continental shelves. *Nature Communications*, *9*(1), 3403. https://doi.org/10.1038/s41467-018-05813-1

Naviaux, J. D., Subhas, A. V., Rollins, N. E., Dong, S., Berelson, W. M., & Adkins, J. F. (2019). Temperature dependence of calcite dissolution kinetics in seawater. *Geochimica et Cosmochimica Acta*, *246*, 363–384. https://doi.org/10.1016/j.gca.2018.11.037

Olsen, A., Key, R. M., van Heuven, S., Lauvset, S. K., Velo, A., Lin, X., et al. (2016). The Global Ocean Data Analysis Project version 2 (GLODAPv2)––An internally consistent data product for the world ocean. *Earth System Science Data*, *8*(2), 297–323. https://doi.org/10.5194/essd-8-297-2016

Ott, L. E., Pawson, S., Collatz, G. J., Gregg, W. W., Menemenlis, D., Brix, H., et al. (2015). Assessing the magnitude of $CO_2$ flux uncertainty in atmospheric $CO_2$ records using products from NASA's carbon monitoring flux pilot project. *Journal of Geophysical Research: Atmospheres*, *120*, 734–765. https://doi.org/10.1002/2014JD022411

Parekh, P., Follows, M. J., & Boyle, E. A. (2005). Decoupling of iron and phosphate in the global ocean. *Global Biogeochemical Cycles*, *19*, GB2020. https://doi.org/10.1029/2004GB002280

Pfeil, B., Olsen, A., Bakker, D. C. E., Hankin, S., Koyuk, H., Kozyr, A., et al. (2013). A uniform, quality-controlled Surface Ocean $CO_2$ Atlas (SOCAT). *Earth System Science Data*, *5*(1), 125–143. https://doi.org/10.5194/essd-5-125-2013

Redi, M. H. (1982). Oceanic isopycnal mixing by coordinate rotation. *Journal of Physical Oceanography*, *12*(10), 1154–1158. https://doi.org/10.1175/1520-0485(1982)012<1154:OIMBCR>2.0.CO;2

Resplandy, L., Keeling, R. F., Rödenbeck, C., Stephens, B. B., Khatiwala, S., Rodgers, K. B., et al. (2018). Revision of global carbon fluxes based on a reassessment of oceanic and riverine carbon transport. *Nature Geoscience*, *11*(7), 504–509. https://doi.org/10.1038/s41561-018-0151-3

Reynolds, R. W., Rayner, N. A., Smith, T. M., Stokes, D. C., & Wang, W. (2002). An improved in situ and satellite SST analysis for climate. *Journal of Climate*, *15*(13), 1609–1625. https://doi.org/10.1175/1520-0442(2002)015<1609:AIISAS>2.0.CO;2

Riebesell, U., Schulz, K. G., Bellerby, R. G. J., Botros, M., Fritsche, P., Meyerhö, M., et al. (2007). Enhanced biological carbon consumption in a higher $CO_2$ ocean. *Nature*, *450*(7169), 545–548. https://doi.org/10.1038/nature06267

Riser, S. C., Freeland, H. J., Roemmich, D., Wijffels, S., Troisi, A., Belbéoch, M., et al. (2016). Fifteen years of ocean observations with the global Argo array. *Nature Climate Change*, *6*(2), 145–153. https://doi.org/10.1038/nclimate2872

Riser, S. C., Swift, D., & Drucker, R. (2018). Profiling floats in SOCCOM: Technical capabilities for studying the Southern Ocean. *Journal of Geophysical Research: Oceans*, *123*, 4055–4073. https://doi.org/10.1002/2017JC013419

Ritter, R., Landschützer, P., Gruber, N., Fay, A. R., Iida, Y., Jones, S., & Zeng, J. (2017). Observation-based trends of the Southern Ocean carbon sink. *Geophysical Research Letters*, *44*, 339–348. https://doi.org/10.1002/2017GL074837

Rödenbeck, C., Bakker, D. C. E., Gruber, N., Iida, Y., Jacobson, A. R., Jones, S., et al. (2015). Data-based estimates of the ocean carbon sink variability—First results of the Surface Ocean $p$CO$_2$ Mapping intercomparison (SOCOM). *Biogeosciences*, *12*(23), 7251–7278. https://doi.org/10.5194/bg-12-7251-2015

Rödenbeck, C., Keeling, R. F., Bakker, D. C. E., Metzl, N., Olsen, A., Sabine, C., & Heimann, M. (2013). Global surface-ocean $p$CO$_2$ and sea-air $CO_2$ flux variability from an observation-driven ocean mixed-layer scheme. *Ocean Science*, *9*(2), 193–216. https://doi.org/10.5194/os-9-193-2013

Roemmich, D., & Gilson, J. (2009). The 2004–2008 mean and annual cycle of temperature, salinity, and steric height in the global ocean from the Argo program. *Progress in Oceanography*, *82*(2), 81–100. https://doi.org/10.1016/j.pocean.2009.03.004

Roquet, F., Wunsch, C., Forget, G., Heimbach, P., Guinet, C., Reverdin, G., et al. (2013). Estimates of the Southern Ocean general circulation improved by animal-borne instruments. *Geophysical Research Letters*, *40*, 6176–6180. https://doi.org/10.1002/2013GL058304

Sabine, C. L., Feely, R. A., Gruber, N., Key, R. M., Lee, K., Bullister, J. L., et al. (2004). The oceanic sink for anthropogenic $CO_2$. *Science*, *305*(5682), 367–371. https://doi.org/10.1126/science.1097403

Sarmiento, J. L., Dunne, J., Gnanadesikan, A., Key, R. M., Matsumoto, K., & Slater, R. (2002). A new estimate of the $CaCO_3$ to organic carbon export ratio. *Global Biogeochemical Cycles*, *16*(4), PA001515. https://doi.org/10.1029/2002GB001919

Sarmiento, J. L., & Gruber, N. (2002). Sinks for anthropogenic carbon. *Physics Today*, *55*(8), 30–36. https://doi.org/10.1063/1.1510279

Sarmiento, J. M., Gloor, M., Gruber, N., Beaulieu, C., Jacobson, A. R., Mikaloff Fletcher, S. E., et al. (2010). Trends and regional distributions of land and ocean carbon sinks. *Biogeosciences*, *7*(8), 2351–2367. https://doi.org/10.5194/bg-7-2351-2010

Sausen, R., Barthel, K., & Hasselmann, K. (1988). Coupled ocean-atmosphere models with flux correction. *Climate Dynamics*, *2*(3), 145–163. https://doi.org/10.1007/BF01053472

Schuster, U., McKinley, G. A., Bates, N., Chevallier, F., Doney, S. C., Fay, A. R., et al. (2013). An assessment of the Atlantic and Arctic sea-air $CO_2$ fluxes, 1990–2009. *Biogeosciences*, *10*(1), 607–627. https://doi.org/10.5194/bg-10-607-2013

Semiletov, I., Makshtas, A., Akasofu, S. I., & Andreas, E. (2004). Atmospheric $CO_2$ balance: The role of Arctic Sea ice. *Geophysical Research Letters*, *31*, L05121. https://doi.org/10.1029/2003GL017996

Stammer, D., Ueyoshi, K., Köhl, A., Large, W. G., Josey, S. A., & Wunsch, C. (2004). Estimating air-sea fluxes of heat, freshwater, and momentum through global ocean data assimilation. *Journal of Geophysical Research*, *109*, C05023. https://doi.org/10.1029/2003JC002082

Stock, C. A., Dunne, J. P., & John, J. G. (2014). Global-scale carbon and energy flows through the marine planktonic food web: An analysis with a coupled physical–biological model. *Progress in Oceanography*, *120*, 1–28. https://doi.org/10.1016/j.pocean.2013.07.001

Subhas, A. V., Rollins, N. E., Berelson, W. M., Dong, S., Erez, J., & Adkins, J. F. (2015). Novel determination of the dissolution kinetics of inorganic calcite in seawater. *Geochimica et Cosmochimica Acta*, *170*, 51–68. https://doi.org/10.1016/j.gca.2015.08.011

Takahashi, T., Sutherland, S. C., Sweeney, C., Poisson, A., Metzl, N., Tilbrook, B., et al. (2002). Global Sea-air $CO_2$ flux based on climatological surface ocean $p$CO_2, and seasonal biological and temperature effects. *Deep Sea Research, Part II*, *49*(9-10), 1601–1622. https://doi.org/10.1016/S0967-0645(02)00003-6

Takahashi, T., Sutherland, S. C., Wanninkhof, R., Sweeney, C., Feely, R. A., Chipman, D. W., et al. (2009). Climatological mean and decadal change in surface ocean $p$CO_2, and net sea-air $CO_2$ flux over the global oceans. *Deep Sea Research, Part II*, *56*(8–10), 554–577. https://doi.org/10.1016/j.dsr2.2008.12.009

Treasure, A., Roquet, F., Ansorge, I., Bester, M., & Boehme, L. (2017). Marine mammals exploring the oceans pole to pole: A review of the MEOP consortium. *Oceanography*, *30*(2), 132–138. https://doi.org/10.5670/oceanog.2017.234

Tziperman, E., & Thacker, W. C. (1989). An optimal-control/adjoint-equations approach to studying the oceanic general circulation. *Journal of Physical Oceanography*, *19*, 1471–1485. https://doi.org/10.1175/1520-0485(1989)019<1471:aoceat>2.0.co;2

Verdy, A., & Mazloff, M. R. (2017). A data assimilating model for estimating Southern Ocean biogeochemistry. *Journal of Geophysical Research: Oceans*, *122*, 6968–6988. https://doi.org/10.1002/2016JC012650

Wanninkhof, R. (1992). Relationship between wind speed and gas exchange over the ocean. *Journal of Geophysical Research*, *97*(C5), 7373–7382. https://doi.org/10.1029/92JC00188

Wanninkhof, R., Park, G. H., Takahashi, T., Sweeney, C., Feely, R., Nojiri, Y., et al. (2013). Global Ocean carbon uptake: Magnitude, variability and trends. *Biogeosciences*, *10*(3), 1983–2000. https://doi.org/10.5194/bg-10-1983-2013

Watkins, M., Wiese, D., Yuan, D., Boening, C., & Landerer, F. (2015). Improved methods for observing Earth's time variable mass distribution with GRACE using spherical cap mascons. *Journal of Geophysical Research: Solid Earth*, *120*, 2648–2671. https://doi.org/10.1002/2014JB011547

Wood, M., Rignot, E., Fenty, I. G., Menemenlis, D., Millan, R., Morlighem, M., et al. (2018). Ocean-induced melt triggers glacier retreat in Northwest Greenland. *Geophysical Research Letters*, *45*, 8334–8342. https://doi.org/10.1029/2018GL078024

Wunsch, C., & Heimbach, P. (2013). Dynamically and kinematically consistent global ocean circulation and ice state estimates. In G. Siedler, S. M. Griffies, J. Gould, & J. A. Church (Eds.), *Ocean Circulation and Climate: A 21st Century Perspective* (Vol. 103, pp. 553-579). New York, NY: Academic Press. https://doi.org/10.1016/B978-0-12-391851-2.00021-0

Wunsch, C., Heimbach, P., Ponte, R., & Fukumori, I. (2009). The global general circulation of the ocean estimated by the ECCO-consortium. *Oceanography*, *22*(2), 88–103. https://doi.org/10.5670/oceanog.2009.41

Yue, S., Pilon, P., & Cavadias, G. (2002). Power of the Mann-Kendall and Spearman's rho tests for detecting monotonic trends in hydrological series. *Journal of Hydrology*, *264*(1-4), 262–263. https://doi.org/10.1016/S0022-1694(02)00078-1

Zhang, H., Menemenlis, D., & Fenty, I. G. (2018). ECCO LLC270 ocean-ice state estimate, http://hdl.handle.net/1721.1/119821

## References From the Supporting Information

de Boyer Montégut, C., Madec, G., Fischer, A. S., Lazar, A., & Iudicone, D. (2004). Mixed layer depth over the global ocean: An examination of profile data and a profile-based climatology. *Journal of Geophysical Research*, *109*, C12003. https://doi.org/10.1029/2004JC002378

Krakauer, N. Y., Randerson, J. T., Primeau, F. W., Gruber, N., & Menemenlis, D. (2006). Carbon isotope evidence for the latitudinal distribution and wind speed dependence of the air-sea gas transfer velocity. *Tellus*, *58B*, 390–417. https://doi.org/10.1111/j.1600-0889.2006.00223.x